Calibrating an Ice Sheet Model using High-dimensional Binary Spatial Data

Won Chang, Murali Haran, Patrick Applegate, David Pollard

July 29, 2021

Abstract

Rapid retreat of ice in the Amundsen Sea sector of West Antarctica may cause drastic sea level rise, posing significant risks to populations in low-lying coastal regions. Calibration of computer models representing the behavior of the West Antarctic Ice Sheet is key for informative projections of future sea level rise. However, both the relevant observations and the model output are high-dimensional binary spatial data; existing computer model calibration methods are unable to handle such data. Here we present a novel calibration method for computer models whose output is in the form of binary spatial data. To mitigate the computational and inferential challenges posed by our approach, we apply a generalized principal component based dimension reduction method. To demonstrate the utility of our method, we calibrate the PSU3D-ICE model by comparing the output from a 499-member perturbed-parameter ensemble with observations from the Amundsen Sea sector of the ice sheet. Our methods help rigorously characterize the parameter uncertainty even in the presence of systematic data-model discrepancies and dependence in the errors. Our method also helps inform environmental risk analyses by contributing to improved projections of sea level rise from the ice sheets.

1 Introduction

Mass loss from the polar ice sheets has the potential to make substantial contributions to future sea level rise. The ice sheets therefore pose substantial risks to people living near present sea level. Taken together, the ice sheets contain sufficient ice to raise global mean sea level by up to 60 meters if they were to melt completely; the West Antarctic Ice Sheet (WAIS) might

contribute up to 4 meters to future sea level rise (Fretwell et al., 2013), whereas the Greenland and East Antarctic Ice Sheets might contribute up to 7 meters and up to 50 meters to sea level rise, respectively. Recent observations of increased surface air temperatures at high northern latitudes, and warmer ocean waters at high southern latitudes, suggest that some fraction of this ice may melt over the next few decades or centuries (Zhang, 2007; Serreze and Barry, 2011). Geologic observations also indicate that the ice sheets can make rapid contributions to sea level (e.g., Deschamps et al., 2012). A significant fraction of the world's population lives near present sea level (Nicholls et al., 2008), and these people will face an increased risk from storm surges as sea level rise progresses. The future behavior of the ice sheets is hence a key input for risk analyses (e.g., Lempert et al., 2012).

Despite the ice sheets' importance for future sea level rise, projecting their future behavior using computer models remains challenging. In contrast to global climate models, which represent the behavior of the atmosphere, oceans, vegetation, and other parts of the Earth system, ice sheet models typically include advanced treatments of ice flow and simplified representations of the boundary conditions at the ice sheets' interfaces with the atmosphere and oceans. Until recently, many ice sheet models lacked realistic representations of processes that may play an important role in the ice sheets' future development (e.g., Little et al., 2007). Recent studies (see, e.g. Stone et al., 2010; Applegate et al., 2012) confirm that imperfect knowledge of model input parameters leads to large uncertainties in modeled sea level contributions. Thus, characterizing and reducing parametric uncertainty is a key step in producing ice sheet projections that can properly inform climate risk analyses.

Calibration of ice sheet models is challenging because the relevant data are high-dimensional binary spatial data, and the models themselves are computationally expensive. Recent efforts to calibrate ice sheet models include Gladstone et al. (2012), McNeall et al. (2013), and Chang et al. (2014a). These studies represent significant advances in the state of the art for ice sheet model calibration, but each has significant limitations. Gladstone et al. (2012) uses a heuristic approach which chooses input parameter settings that yield output values which fall in the 95% confidence set. The confidence set is defined by the 'three-sigma rule' (Pukelsheim, 1994), choosing the margin of errors for the confidence sets as ± 3 standard errors, and a Bonferroni-type multiple test procedure to generalize it to the multivariate case. The approach ensures robustness against assumptions about the model-observation discrepancy and the observational errors. The framework requires running the ice sheet model for at least thousands of parameter

settings and hence is applicable only to heavily simplified ice sheet models such as the one-dimensional flow-line model used by Gladstone et al. (2012). McNeall et al. (2013) uses a Gaussian process emulator for three quantities: the overall ice volume, the maximum ice height, and the area covered by ice. The use of Gaussian process emulators makes this approach computationally feasible, even with computationally expensive 3-D ice-sheet models. However, their analysis is based on heavily aggregated quantities and therefore does not utilize spatially resolved information. Moreover, instead of utilizing the probability model given by the emulator, they rely on a heuristic approach based on an "implausibility measure", which is the model output mean standardized using the observational data. The approach in Chang et al. (2014a) improves upon these two approaches by using the probabilistic calibration approach proposed by Kennedy and O'Hagan (2001) and extended and generalized by many others (see, e.g. Kennedy and O'Hagan, 2001; Bayarri et al., 2007; Higdon et al., 2008).

However, current calibration approaches are unable to utilize important sources of information about ice sheet behavior such as the extent of ice covered area in modern- and paleo-observations (Alley et al., 2010) due to the binary nature of the model output and observations. For example, some Greenland ice cores contain ice from the last interglacial period (from 125,000 years ago), whereas others do not; however, rigorous calibration approaches that can take this type of data into account are lacking. Chang et al. (2014a) circumvents this problem by using datasets obtained by aggregating the 2-dimensional spatial pattern of ice thickness into a 1-dimensional profile to make the data more suitable for Gaussian process-based approaches and hence is silent on using datasets that are in the form of non-Gaussian spatial processes. Aggregating data in this manner likely results in significantly larger projection uncertainties than would result if unaggregated data were used (Chang et al., 2014b). Thus, more work to properly incorporate binary spatial data into ice sheet model calibration is needed.

Here we propose a new calibration approach for high-dimensional binary spatial data, appropriate for calibration of ice sheet models using data on the spatial pattern of ice coverage. The spatial data that we use here are gridded binary patterns, where the outcome at each location represents absence or presence of grounded ice. Our novel calibration approach extends the Gaussian process-based calibration framework to high-dimensional binary spatial data. Our approach is based on a generalized linear model framework with a latent Gaussian process. To mitigate the considerable computational challenges posed by the high-dimensional latent process, we reduce the dimensionality of the model output and the data using a logistic principal

3

component analysis (Collins et al., 2002; Lee et al., 2010). This approach avoids inference with high-dimensional latent variables while also sidestepping the computational burden posed by high-dimensional matrix computations.

We use this approach to calibrate an innovative ice sheet model (PSU3D-ICE; see below), using data on the spatial extent of grounded ice (i.e., binary pattern of presence and absence of grounded ice) within the Amundsen Sea sector of the West Antarctic Ice Sheet. The Amundsen Sea sector is likely the largest contributor to sea level rise of any Antarctic ice drainage (Pritchard et al., 2012). It includes the rapidly thinning Pine Island and Thwaites Glaciers, which drain ice from the interior of the West Antarctic Ice Sheet into the ocean. The glaciers terminate in ice shelves where the grounded ice becomes too thin to remain in contact with the seafloor. Ice velocities are high within the glacier trunks, but slow elsewhere. The position of the grounding line, or the narrow region separating the grounded ice from the floating ice shelves, is known from modern geophysical measurements (Fretwell et al., 2013).

The Pennsylvania State University three-dimensional ice sheet model, PSU3D-ICE, simulates the combined ice sheet-ice shelf system using a so-called "hybrid" dynamical core, which smoothly merges the shallow-shelf and shallow-ice approximations to the Stokes equations describing ice flow (Kirchner et al., 2011). This approach allows the model to simulate the full ice sheet-ice shelf system realistically, while minimizing the computational cost of the model. Pollard and DeConto (2009, 2012b,a) provide detailed descriptions of the model, which has been part of several ice-sheet model intercomparisons (e.g., seaRISE, Bindschadler et al., 2013).

The remainder of this paper is organized as follows. In Section 2 we describe the model output and the observational data that we use in our analysis. In Section 3 we introduce the basic framework for calibration using binary spatial data and explain the computational challenges posed by high-dimensional spatial data. We formulate a reduced-dimensional approach to mitigate these challenges in Section 4. We describe how to compute the logistic principal components (PCs) for binary computer model output and formulate an emulation framework based on them, and then set up a calibration model that relies on the reduced-dimensional emulator. Section 5 describes the implementation details and results for our experiments on a simulated example as well as the application of our methods to the ice sheet model for WAIS described in Section 2. We also discuss the preliminary implications of our research on the study of the behavior of the West Antarctic Ice Sheet. We conclude this paper with a summary and future directions in Section 6.

2 Model Description and Observational Data

We use an innovative 3-D ice-sheet model, which uses boundary-layer techniques to capture challenging grounding-zone dynamics while still being efficient enough to feasibly perform long-term simulations. Basically the model simulates the long-term evolution of ice extent and thickness, changing due to slow deforming flow and basal sliding under its own weight, surface snowfall and melt, ocean melting under floating ice shelves, and iceberg calving, over the Antarctic continent. For the simulations in this manuscript, the model is applied to a nested domain spanning West Antarctica, with a relatively fine grid resolution of 20 km. This nested grid is driven at its lateral boundaries by stored results from a previous coarser-scale continental simulation.

The model is run over the last 40,000 years, initialized appropriately at 40 ka (40,000 years Before Present or BP, relative to 1950 AD) from a previous long-term run. Atmospheric forcing is supplied using a modern climatological Antarctic dataset (ALBMAP: Le Brocq, A.M. and Payne, A.J. and Vieli, A., 2010), with uniform cooling perturbations applied proportional to a deep-sea-core $\delta^{18}O$ record (Pollard and DeConto, 2009, 2012a). Oceanic forcing is supplied using archived ocean temperatures from a coupled AOGCM simulation of the last 20 kyr (1 kyr=1,000 years) (Liu et al., 2009b). Sea level versus time, rising during this period primarily due to Northern Hemispheric ice-sheet melt, is prescribed from the ICE-5G dataset (Peltier, 2004). Modern bedrock elevations are obtained from the Bedmap2 dataset (Fretwell et al., 2013).

After reaching present day (0 ka), each run is extended for 5,000 years with a very basic representation of future warming. Atmospheric and oceanic temperatures are uniformly increased by 6 and 2 °C, respectively, ramped up linearly from 0 to 150 years after present and held constant thereafter. Ocean-temperature increases are confined to a longitudinal sector around the Amundsen Sea Embayment of West Antarctica, corresponding to the location of observed sub-ice melt increases in recent decades. This simple prescription of future temperature changes causes drastic ice retreat into the West Antarctic interior in many of the runs. More realistic future warming scenarios are planned for future work. Other aspects of the model are described in Pollard and DeConto (2012b,a).

All 3-D ice sheet models have a number of poorly constrained internal parameters. To evaluate the effects of these uncertain parameters in the PSU3D-ICE model, we selected 10 highly uncertain parameters to vary in a Latin hypercube (LHC) ensemble (Table 1). LHC

design (see, e.g. McKay et al., 1979; Stein, 1987) allows us to explore a reasonably wide range of parameter values with a relatively smaller number of model runs even with a high-dimensional parameter space. We use a random LHC design generated by 'lhc' package in R (Carnell, 2012). While a random LHC can result in a design with highly correlated input parameter values (cf. Joseph and Hung, 2008), we have confirmed that in our design the correlation coefficients between the parameter values are very low (all less than 0.08). Four of these parameters are generally recognized as particularly important, with strong effects on past and present ice configurations, but which represent uncertain processes in glaciology. See Section 5.2 for a description of these parameters. Each parameter value is remapped to the $[0, 1]$ interval with 0.5 generally being the non-statistically tuned value by previous research (Pollard and DeConto, 2012a; Pollard et al., 2015) and 499 design points for the input parameters are chosen by LHC design for the 10-dimensional unit cube.

We calibrate the model by inferring these ten parameters using the observed modern day grounding-line geometry, i.e., the modern "coastline" map of grounded ice versus floating ice, from a modern Antarctic dataset (Bedmap2; Fretwell et al., 2013). The original model output covers the entire WAIS, but we use a subset of the output that corresponds to the observational data for ASE (Amundsen Sea Embayment). The spatial pattern for each parameter setting and the observational data has 86×37 regular grid points. At each grid cell, we have a binary outcome with 1 representing presence of grounded ice and 0 representing absence of grounded ice. See Figure 1 for the observational data and an example model output. Note that both the model output and the observational data are in the form of high-dimensional and binary spatial patterns; the challenges posed by these data structures will drive much of our methods development in the following sections.

3   Computer Model Emulation and Calibration Using Binary Spatial Data

In this section, we introduce a framework for computer model emulation and calibration with Gaussian spatial data and then describe our new approach for emulation-calibration with binary spatial data. We follow the two-stage approach to computer model calibration (Bayarri et al., 2007; Bhat et al., 2012; Chang et al., 2014b, 2015). In the two stage approach, the computer model is first approximated using a Gaussian process emulator, and then in the calibration step,

the model parameters are inferred based on observational data using the emulator. Separating the emulation step from the calibration step makes it easier to diagnose the performance of the emulator and improves the identifiability of the parameters in the calibration model (see Rougier, 2008; Bhat et al., 2010, 2012, for more discussion). Here the computer model output is in the form of binary spatial data, and we specify a generalized linear model framework and formulate an emulator that interpolates natural parameters across the model input settings using a Gaussian process. For the calibration step we introduce a model for data-model discrepancy and model the natural parameters for the observational data using the constructed emulator and the discrepancy model. When the model output is in the form of Gaussian spatial data, there is a possibility that we underestimate the parametric uncertainty when we do not account for the uncertainty in the estimated emulator parameters (see for instance, Bayarri et al., 2007; Bhat et al., 2012; Liu et al., 2009a; Chang et al., 2014b). However, when the model output is in the form of binary spatial data, based on several simulated examples we find that we do not underestimate the parametric uncertainty. In fact, allowing uncertainties for this parameters leads to identifiability issues in the inference in the calibration stage.

Computation presents considerable challenges. We therefore propose a principal components-based framework in order to make our approach computationally feasible. To help set the stage for the description of our framework for emulation and calibration in this manuscript, we begin with a description of emulation-calibration using Gaussian spatial data in Section 3.1. This framework is also described in Kennedy and O'Hagan (2001); Bayarri et al. (2007); Higdon et al. (2008); Bhat et al. (2012); Chang et al. (2014b). Sections 3.2 and 3.3 provide details about our framework for emulation and calibration for binary spatial model output and observational data. Section 3.4 describes the computational and inferential challenges, and Section 4 provides details about our computationally expedient reduced-dimension approach to mitigate these challenges.

We use the following notation henceforth. Let $Y(\boldsymbol{\theta}, \mathbf{s})$ be the computer model output at a parameter setting $\boldsymbol{\theta} \in \boldsymbol{\Theta}$ and a spatial location $\mathbf{s} \in \mathcal{S}$ where $\boldsymbol{\Theta} \subset R^d$ is the parameter space and $\mathcal{S}$ is the spatial field that covers the geographical area of interest. The integer d represents the number of input parameters that the computer model has. We assume that we have obtained model runs at p design points $\boldsymbol{\theta}_1, \ldots, \boldsymbol{\theta}_p \in \boldsymbol{\Theta}$ and each model run has n spatial locations $\mathbf{s}_1, \ldots, \mathbf{s}_n \in \mathcal{S}$. We let $\mathbf{Y}$ be a $p \times n$ matrix of the computer model output where the (i, j)th element $Y(\boldsymbol{\theta}_i, \mathbf{s}_j)$ is the model output at the ith parameter setting $\boldsymbol{\theta}_i$ and the jth spatial

location $\mathbf{s}_j$. Similarly, let $\mathbf{Z}$ be the n-dimensional observational data where its jth element $Z(\mathbf{s}_j)$ is the observation at the jth spatial location $\mathbf{s}_j$. For the ice sheet model calibration example in Section 5.2, $p = 499$ and $n = 86 \times 37 = 3,182$.

3.1 Computer Model Emulation and Calibration Using Gaussian Spatial Data

We briefly outline emulation and calibration for Gaussian spatial data (cf. Bhat et al., 2010, 2012; Chang et al., 2014b, 2015). The purpose of this subsection is to make it easier for readers to follow the remainder of this section. Here we assume that $Y(\boldsymbol{\theta}, \mathbf{s})$ can be reasonably modeled by a Gaussian distribution. In the emulation stage, we fit the following Gaussian process model for the computer model output $\mathbf{Y}$ to interpolate the values at the parameter settings $\boldsymbol{\theta}_1, \ldots, \boldsymbol{\theta}_p$ and the spatial locations $\mathbf{s}_1, \ldots, \mathbf{s}_n$ simultaneously:

$$\text{vec}\,(\mathbf{Y}) \sim N(\mathbf{X}\boldsymbol{\beta}, \boldsymbol{\Sigma}(\boldsymbol{\xi}_y)), \tag{1}$$

where vec$(\cdot)$ is the vectorization operator that concatenates columns into one vector. The $np \times b$ matrix $\mathbf{X}$ contains values of b different covariates that can be used to represent general trends in the model output. The $np \times np$ covariance matrix $\boldsymbol{\Sigma}(\boldsymbol{\xi}_y)$ with a vector of parameters $\boldsymbol{\xi}_y$ is defined by a positive definite covariance function for a Gaussian process (see, e.g. Sacks et al., 1989) that interpolates between the model output at different parameter settings $\boldsymbol{\theta}_1, \ldots, \boldsymbol{\theta}_p$ and spatial locations $\mathbf{s}_1, \ldots, \mathbf{s}_n$. In general, the mean term $\mathbf{X}\boldsymbol{\beta}$ can be set to $\mathbf{0}$ with a proper centering of $\mathbf{Y}$, and the covariance parameters in $\boldsymbol{\xi}_y$ can be estimated by the maximum likelihood estimate $\hat{\boldsymbol{\xi}}_y$.

In the calibration step, we model the observational data using the following model:

$$\mathbf{Z} = \boldsymbol{\eta}(\boldsymbol{\theta}, \mathbf{Y}) + \boldsymbol{\delta},$$

where $\boldsymbol{\eta}(\boldsymbol{\theta}, \mathbf{Y})$ is the n-dimensional emulated vector, a computer model output approximated by interpolating the model runs in $\mathbf{Y}$ using the model in (1), and $\boldsymbol{\delta} \sim N(\mathbf{0}, \boldsymbol{\Sigma}(\boldsymbol{\xi}_d))$ is an n-dimensional spatially correlated zero-mean Gaussian vector with covariance parameter $\boldsymbol{\xi}_d$ that represents the systematic model-observation discrepancy. By choosing standard priors for the parameters in the model, one can infer $\boldsymbol{\theta}$ via Markov Chain Monte Carlo (MCMC) along with other parameters.

3.2 Computer Model Emulation Using Binary Spatial Model Output

In this section and for the remainder of this paper, we assume that $Y(\boldsymbol{\theta}, \mathbf{s})$ is binary with 0-1 values. We assume the model output $Y(\boldsymbol{\theta}_i, \mathbf{s}_j)$ to be a Bernoulli random variable with success probability $p_{ij} = P(Y(\boldsymbol{\theta}_i, \mathbf{s}_j) = 1)$. We denote the corresponding logit $\log\left(\frac{p_{ij}}{1-p_{ij}}\right)$ by γ_{ij} and hence the probability mass function for $Y(\boldsymbol{\theta}_i, \mathbf{s}_j)$ can be written as

$$
\begin{aligned}
P(Y(\boldsymbol{\theta}_i, \mathbf{s}_j) = y_{ij}) &= p_{ij}^{y_{ij}}(1 - p_{ij})^{1-y_{ij}} \\
&= \left(\frac{\exp(\gamma_{ij})}{1 + \exp(\gamma_{ij})}\right)^{y_{ij}} \left(\frac{1}{1 + \exp(\gamma_{ij})}\right)^{1-y_{ij}} \\
&= (1 + \exp(-(2y_{ij} - 1)\gamma_{ij}))^{-1}.
\end{aligned}
$$

We let $\boldsymbol{\Gamma}$ be the $p \times n$ matrix of natural parameters for model output, where its (i,j)th element is γ_{ij}. By assuming that the elements in the model output $\mathbf{Y}$ are conditionally independent given the natural parameters in $\boldsymbol{\Gamma}$, the likelihood function for the model output $\mathbf{Y}$ can be written as follows;

$$
L(\mathbf{Y}|\boldsymbol{\Gamma}) = \prod_{i=1}^{p}\prod_{j=1}^{n} P(Y(\boldsymbol{\theta}_i, \mathbf{s}_j) = y_{ij}) = \prod_{i=1}^{p}\prod_{j=1}^{n}(1 + \exp(-(2y_{ij} - 1)\gamma_{ij}))^{-1}. \tag{2}
$$

The dependence among the elements in $\mathbf{Y}$ is modeled through the dependence among the elements in $\boldsymbol{\Gamma}$. To approximate the computer model we interpolate the natural parameters at different input parameter settings using a Gaussian process (cf. Sacks et al., 1989) with zero mean and a covariance function that depends on the input parameter settings and the spatial locations for model output, i.e.,

$$
\mathrm{Cov}\left(\gamma_{ij}, \gamma_{kl}\right) = C\left(\boldsymbol{\theta}_i, \boldsymbol{\theta}_k, \mathbf{s}_j, \mathbf{s}_l; \boldsymbol{\xi}_y\right), \tag{3}
$$

where C is a valid covariance function over $(\Theta \times \mathcal{S})^2$ and $\boldsymbol{\xi}_y$ is a vector of covariance parameters. Note that estimating the natural parameters $\{\gamma_{ij}, i = 1 \ldots, p, j = 1, \ldots, n\}$ is not possible by simply maximizing (2) since this is an ill-posed problem without any constraints on them (see Section 3.4 for details). If estimates of the natural parameters are available, we can fit the Gaussian process to those natural parameters by maximizing the likelihood function corresponding to the probability model

$$
\mathrm{vec}\left(\boldsymbol{\Gamma}\right) \sim N(\mathbf{0}, \boldsymbol{\Sigma}(\boldsymbol{\xi}_y))
$$

with respect to $\boldsymbol{\xi}_y$, where the covariance matrix $\boldsymbol{\Sigma}(\boldsymbol{\xi}_y)$ is given by a function of the form in (3). We then use the fitted process to predict the vector of natural parameters at any new parameter value $\boldsymbol{\theta}$. We call the fitted Gaussian process an "emulator" and the resulting predictive process an "emulator process".

3.3 Computer Model Calibration Using Binary Spatial Data

Again, in this section and for the remainder of this paper, we assume that $Z(\mathbf{s})$ is binary with 0-1 values. We set up a calibration model that links the input parameter to the observational data using the emulator constructed in the previous section while considering the systematic discrepancy. Let $\boldsymbol{\lambda} = (\lambda_1, \ldots, \lambda_n)^T$ be the n-dimensional vector of natural parameters for the observational data, then our calibration model is given by

$$\boldsymbol{\lambda} = \boldsymbol{\eta}\left(\boldsymbol{\theta}, \mathbf{Y}\right) + \boldsymbol{\delta}, \tag{4}$$

where $\boldsymbol{\delta}$ is an n-dimensional vector for the model-observation discrepancy. Here we can think of $\boldsymbol{\theta}$ as a "fitted" value for the parameter $\boldsymbol{\theta}$, that is, $\boldsymbol{\theta}$ at which the values of the natural parameters match those from which the observations are assumed to originate. For $\boldsymbol{\delta}$ we use an n-dimensional Gaussian random vector with covariance parameters $\boldsymbol{\xi}_d$ that is independent of the emulator process $\boldsymbol{\eta}\left(\boldsymbol{\theta}, \mathbf{Y}\right)$. This corresponds to the following probability model for each observation given by the standard logistic regression framework:

$$\begin{aligned} P(Z(\mathbf{s}_j) = z_j) &= \left(\frac{\exp(\lambda_j)}{1 + \exp(\lambda_j)}\right)^{z_j} \left(\frac{1}{1 + \exp(\lambda_i)}\right)^{1 - z_j} \\ &= (1 + \exp(-(2z_j - 1)\lambda_j))^{-1}, \end{aligned} \tag{5}$$

where λ_j is the jth element of $\boldsymbol{\lambda}$. The log-likelihood function for $\boldsymbol{\lambda}$, $\boldsymbol{\theta}$, and $\boldsymbol{\xi}_d$ given $\boldsymbol{\Gamma}$ and $\mathbf{Z}$ can be written as

$$\ell(\mathbf{Z}, \boldsymbol{\Gamma} | \boldsymbol{\lambda}, \boldsymbol{\theta}, \boldsymbol{\xi}_d) = \ell\left(\boldsymbol{\Gamma} | \boldsymbol{\lambda}, \boldsymbol{\theta}, \boldsymbol{\xi}_d\right) + \ell\left(\mathbf{Z} | \boldsymbol{\lambda}\right).$$

Here $\ell\left(\boldsymbol{\Gamma} | \boldsymbol{\lambda}, \boldsymbol{\theta}, \boldsymbol{\xi}_d\right)$ and $\ell\left(\mathbf{Z} | \boldsymbol{\lambda}\right)$ are given by the probability models in (4) and (5) respectively. With a standard prior specification for the input parameters $\boldsymbol{\theta}$, the discrepancy parameters in $\boldsymbol{\xi}_d$, and the latent process $\boldsymbol{\lambda}$, we can define the posterior density for those parameters and carry out Bayesian inference using MCMC.

3.4 Computational Challenges

The framework described above faces computational and inferential challenges when the number of spatial locations n is large. The emulation step described in Section 3.2 requires estimation of np natural parameters. This is an ill-posed problem since the number of data points in the model output is also np. It is not straightforward to find a set of constraints that leads to well-posed parameter inference while still allowing enough flexibility for the resulting process. Even if estimates of the natural parameters are available, emulation still poses significant computational challenges. Emulation involves numerically finding the maximum likelihood estimate of $\boldsymbol{\xi}_y$, requiring repeated evaluation of a computationally infeasible likelihood function; each likelihood evaluation here involves Cholesky decomposition of the $np \times np$ covariance matrix whose computation scales as $\mathcal{O}(n^3 p^3)$. For the example in Section 5, this calculation translates to a computational cost of $\frac{1}{3} \times p^3 \times n^3 = \frac{1}{3} \times 499^3 \times 3,182^3 = 1.33 \times 10^{18}$ flops, which in turn corresponds to at least hundreds of thousands of hours of computing time for a 3.0 Ghz single core. Moreover, storing $np \times np$ double-precision covariance matrix will require $8n^2 p^2 = 8 \times 499^2 \times 3,182^2 = 20,169.33$ terabytes of memory space. The calibration step is subject to similar challenges. Estimating the input parameters $\boldsymbol{\theta}$ and the discrepancy parameters $\boldsymbol{\xi}_d$ requires integrating out the n-dimensional discrepancy process $\boldsymbol{\delta}$, which makes it difficult to construct a well-mixed MCMC algorithm even for a moderate size of n. Moreover, each likelihood evaluation involves Cholesky decomposition of the $n \times n$ covariance matrix and its computational cost scales as $\mathcal{O}(n^3)$. This translates to a computational cost of $\frac{1}{3} \times 3,182^3 = 3.59 \times 10^{10}$ flops in the example in Section 5, which corresponds to 30 minutes of computing time for a 3.0 Ghz single core.

4 Reduced-Dimension Approach for Binary Spatial Data

We propose a reduced-dimension approach to overcome the computational challenges discussed in the previous section. In the emulation step, we build an emulator for the logistic principal components of the model output to solve the inferential issues in estimating np different natural parameters and the computational issues for dealing with the $np \times np$ covariance matrix. Emulation based on principal components helps us to reduce information loss caused by dimension reduction by focusing on the principal directions for the natural parameters that have the maximum variation across the input parameter settings $\boldsymbol{\theta}_1, \ldots, \boldsymbol{\theta}_p$. In the calibration step, we use

11

a basis representation approach to model the discrepancy process, which removes the need to integrate out the n-dimensional discrepancy process and compute the Cholesky decomposition of the $n \times n$ covariance matrix.

4.1 Dimension Reduction for Binary Model Output

In this subsection, we describe the logistic principal component analysis for binary model output in detail by closely following Lee et al. (2010). For dimension reduction we assume that $\mathbf{\Gamma}$ can be written as

$$\mathbf{\Gamma} = \mathbf{1}_p \boldsymbol{\mu}^T + \mathbf{W} \mathbf{K}_y^T, \tag{6}$$

where $\mathbf{K}_y$ is an $n \times J_y$ orthogonal basis matrix, $\mathbf{W}$ is the $p \times J_y$ principal component matrix with (i, j)th element $w_j(\boldsymbol{\theta}_i)$, and $\boldsymbol{\mu}$ is the $n \times 1$ mean vector. We rewrite the likelihood in (2) as

$$L(\mathbf{Y}|\boldsymbol{\mu}, \mathbf{K}_y, \mathbf{W}) = \prod_{i=1}^{p} \prod_{j=1}^{n} g(y_{ij}^*(\mu_j + \mathbf{w}_i \mathbf{k}_{y,j}^T)), \tag{7}$$

where $g(x) = (1 + \exp(-x))^{-1}$, μ_j is the jth element of $\boldsymbol{\mu}$, $y_{ij}^* = 2y_{ij} - 1$, $\mathbf{w}_i$ is the ith row of $\mathbf{W}$, and $\mathbf{k}_{y,j}$ is the jth row of $\mathbf{K}_y$.

Following Lee et al. (2010), we estimate the matrix $\mathbf{W}$ and $\mathbf{K}_y$ by maximizing the likelihood in (7) using the majorization-minimization (MM) algorithm (Lange et al., 2000; Hunter and Lange, 2004). For each iteration of the MM algorithm we minimize the majorizing function instead of the negative likelihood function. The majorizing function is a function that is (i) of the same value as the negative likelihood at the current point of the iteration, (ii) greater than the negative likelihood for all other values of the parameters, and (iii) in an easier form to minimize than the original negative likelihood, such as a quadratic function. As a first step, we note that

$$-\log g(x) \le -\log g(y) - (1 - g(y))(x - y) + \frac{1}{8}(x - y)^2. \tag{8}$$

for any value of y. The equality holds if $x = y$. The proof of this inequality can be found in de Leeuw (2006) (Theorem 4). We can complete the square by adding a term that does not depend on x to rewrite the right hand side as follows;

$$-\log g(x) \le -\log g(y) + \frac{1}{8}\left(x - y - 4\left(1 - g(y)\right)\right)^2. \tag{9}$$

By the fact that y_{ij}^* can take only the value of either +1 or -1, plugging in $y_{ij}^* \gamma_{ij}$ and $y_{ij}^* \gamma_{ij}^{(m)}$

12

into x and y respectively yields

$$-\log g(y_{ij}^*\gamma_{ij}) \leq -\log g(y_{ij}^*\gamma_{ij}^{(m)}) + \frac{1}{8}\left(\gamma_{ij} - x_{ij}^{(m)}\right)^2, \tag{10}$$

where γ_{ij} is the (i,j)th value of $\mathbf{\Gamma}$, $\gamma_{ij}^{(m)}$ is the value of γ_{ij} at the mth iteration, and $x_{ij}^{(m)} = \gamma_{ij}^{(m)} + 4y_{ij}^*(1 - g(y_{ij}^*\gamma_{ij}^{(m)}))$. Note that (6) implies that $\gamma_{ij} = \mu_j + \mathbf{w}_i\mathbf{k}_{y,j}^T$ and $\gamma_{ij}^{(m)} = \mu_j^{(m)} + \mathbf{w}_i^{(m)}\mathbf{k}_{y,j}^{(m)T}$ where $\mu_j^{(m)}$, $\mathbf{k}_{y,j}^{(m)}$, and $\mathbf{w}_i^{(m)}$ are the values of μ_j, $\mathbf{k}_{y,j}$, and $\mathbf{w}_i$ at the mth iteration respectively. Since $-\log g(y_{ij}^*\gamma_{ij}^{(m)})$ does not depend on γ_{ij}, the majoring function for the negative log likelihood function in (7) is given by

$$\sum_{i=1}^{p}\sum_{j=1}^{n}\left(x_{ij}^{(m)} - \mu_j - \mathbf{w}_i\mathbf{k}_{y,j}^T\right)^2.$$

For each iteration the minimum of the majorization function occurs at

$$\mu_j = \frac{1}{p}\sum_{i=1}^{p}\left(x_{ij}^{(m)} - \mathbf{w}_i\mathbf{k}_{y,j}^T\right), \tag{11}$$

$$\mathbf{w}_i = (\mathbf{K}_y^T\mathbf{K}_y)^{-1}\mathbf{K}_y^T(\mathbf{x}_{i.}^{(m)T} - \boldsymbol{\mu}), \tag{12}$$

$$\mathbf{k}_{y,j} = (\mathbf{W}^T\mathbf{W})^{-1}\mathbf{W}^T\left(\mathbf{x}_{.j}^{(m)} - \mathbf{1}_p\mu_j\right), \tag{13}$$

where $\mathbf{x}_{i.}^{(m)}$ and $\mathbf{x}_{.j}^{(m)}$ are the ith row and the jth column of $\mathbf{X}^{(m)}$ respectively and $\mathbf{X}^{(m)}$ is a $p \times n$ matrix having $x_{ij}^{(m)}$ as its (i,j)th element. Cycling through (11) - (13) results in a local maxima of the likelihood function in (7). Results related to convergence for this algorithm can be found in Hunter and Lange (2004). Of course, as in other optimization algorithms one needs to be careful about possible stationary points. We summarize the algorithm as follows.

1. Initialization: Set $m = 1$ and choose starting points $\boldsymbol{\mu}^{(1)} = (\mu_1^{(1)}, \ldots, \mu_n^{(1)})^T$, $\mathbf{W}^{(1)} = \left(\mathbf{w}_1^{(1)T}, \ldots, \mathbf{w}_p^{(1)T}\right)^T$ and $\mathbf{K}_y^{(1)} = \left(\mathbf{k}_{y,1}^{(1)T}, \ldots, \mathbf{k}_{y,n}^{(1)T}\right)^T$.

2. Compute $\gamma_{ij}^{(m)} = \mu_j^{(m)} + \mathbf{w}_i^{(m)}\mathbf{k}_{y,j}^{(m)T}$, $x_{ij}^{(m)} = \gamma_{ij}^{(m)} + 4y_{ij}^*(1 - \pi(y_{ij}^*\gamma_{ij}^{(m)}))$ and let $\mathbf{X}^{(m)} = \left\{x_{ij}^{(m)}\right\}$.

3. Update $\boldsymbol{\mu}^{(m+1)} = \frac{1}{p}\left(\mathbf{X}^{(m)} - \mathbf{W}^{(m)}\mathbf{K}_y^{(m)T}\right)^T\mathbf{1}_p$.

4. Compute $\mathbf{W}^* = (\mathbf{X}^{(m)} - \mathbf{1}_p\boldsymbol{\mu}^{(m+1)T})^T\mathbf{K}_y^{(m)}\left(\mathbf{K}_y^{(m)T}\mathbf{K}_y^{(m)}\right)^{-1}$ and find its singular value decomposition $\mathbf{W}^* = \mathbf{U}\mathbf{\Lambda}\mathbf{V}^T$. Update $\mathbf{W}^{(m+1)} = \mathbf{U}\mathbf{V}^T$.

5. Update $\mathbf{K}_y^{(m+1)} = \left(\mathbf{X}^{(m)} - \mathbf{1}_p\boldsymbol{\mu}^{(m+1)T}\right)^T\mathbf{W}^{(m+1)}$.

6. Set $m + 1$ and repeat from 2 until convergence.

4.2 Emulation Using Logistic PCs

We fit a Gaussian process for each column of $\mathbf{W}$ separately to construct a J_y-dimensional emulator process. We denote the value of the jth principal component as $w_j(\boldsymbol{\theta})$ and set up a Gaussian process for each jth column with the following exponential covariance function for any parameter settings $\boldsymbol{\theta}$ and $\boldsymbol{\theta}'$:

$$\text{Cov}\left(w_j(\boldsymbol{\theta}), w_j(\boldsymbol{\theta}')\right) = \kappa_j \exp\left(-\sum_{i=1}^{d} \frac{|\theta_i - \theta_i'|}{\phi_{ij}}\right) + \zeta_j 1(\boldsymbol{\theta} = \boldsymbol{\theta}'), \tag{14}$$

with the partial sill κ_j, the range parameters ϕ_{ij}, the nugget parameter ζ_j, and the ith element of $\boldsymbol{\theta}$, θ_i. For each jth principal component, we estimate the parameters κ_j, $\phi_{1j}, \ldots, \phi_{dj}$, and ζ_j by maximizing the log likelihood function $\ell(w_j(\boldsymbol{\theta}_1), \ldots, w_j(\boldsymbol{\theta}_p)|\kappa_j, \phi_{1j}, \ldots, \phi_{dj}, \zeta_j)$ given by the Gaussian process for $w_j(\boldsymbol{\theta}_1), \ldots, w_j(\boldsymbol{\theta}_p)$ defined by the covariance function in (14). Here we use the exponential covariance function because we expect that there is not enough information in the binary data to infer the smoothness parameter in Matérn. Our choice of smoothness parameter 0.5 for the Matern covariance function (therefore an exponential covariance function) is a conservative one. We have also conducted a leave-10-percent-out cross validation experiment and found that an emulator with the exponential covariance function shows a better interpolation performance than the squared exponential covariance function. The computational cost for each likelihood evaluation is $\frac{1}{3}p^3$ flops, which is $\frac{1}{3} \times 499^3 \approx 4.14 \times 10^7$ flops in our application.

The J_y-dimensional emulator process $\boldsymbol{\eta}(\boldsymbol{\theta}, \mathbf{W})$ for the logistic PC scores at any new parameter value $\boldsymbol{\theta}$ is obtained as usual from the conditional distribution. Then the n-dimensional emulator process for the natural parameters at $\boldsymbol{\theta}$ is

$$\boldsymbol{\gamma}(\boldsymbol{\theta}) = \boldsymbol{\mu} + \mathbf{K}_y \boldsymbol{\eta}(\boldsymbol{\theta}, \mathbf{W}), \tag{15}$$

and the corresponding probability for the predicted model output at each location to be one is

$$p_j(\boldsymbol{\theta}) = P(Y(\boldsymbol{\theta}, \mathbf{s}_j) = 1) = \frac{\exp(\gamma_j(\boldsymbol{\theta}))}{1 + \exp(\gamma_j(\boldsymbol{\theta}))},$$

where $\gamma_j(\boldsymbol{\theta})$ is the jth element of $\boldsymbol{\gamma}(\boldsymbol{\theta})$ in (15).

4.3 Calibration Using Logistic PCs

Once the emulator for the logistic PCs is available, we set up the following calibration model for the n-dimensional vector of the natural parameters $\boldsymbol{\lambda}$ for observational data using the emulator $\boldsymbol{\mu} + \mathbf{K}_y \boldsymbol{\eta} (\boldsymbol{\theta}, \mathbf{W})$:

$$\boldsymbol{\lambda} = \boldsymbol{\mu} + \mathbf{K}_y \boldsymbol{\eta} + \boldsymbol{\delta}, \tag{16}$$

where $\boldsymbol{\theta}$ is the best fit value for the natural parameters for observational data, $\boldsymbol{\eta} = \boldsymbol{\eta}(\boldsymbol{\theta}, \mathbf{W})$ is the emulated natural parameter vectors at the value of input parameter $\boldsymbol{\theta}$, $\boldsymbol{\delta}$ is the discrepancy term that represents structural error between the natural parameters for the model output and those for the observational data. The intercept $\boldsymbol{\mu}$ and the basis matrix $\mathbf{K}_y$ are given from the emulation stage. To get around the challenges in integrating out $\boldsymbol{\delta}$ described above, we use a basis representation for the discrepancy term such that

$$\boldsymbol{\delta} = \mathbf{K}_d \mathbf{v},$$

with the $n \times J_d$ basis matrix $\mathbf{K}_d$ and the J_d-dimensional random coefficient vector $\mathbf{v} \sim N(\mathbf{0}, \sigma_d^2 \mathbf{I}_{J_d})$. Similar to the independence assumption between the emulated vector and the discrepancy term made for the model in (4), we assume that $(\mathbf{v}, \sigma_d^2)$ is independent of $(\boldsymbol{\eta}, \boldsymbol{\theta}, \mathbf{W})$.

The posterior density given the observational data $\mathbf{Z}$ (see Supplementary Section A1 for details about its derivation) can be written as

$$\pi(\boldsymbol{\eta}, \boldsymbol{\theta}, \mathbf{v}, \sigma_d | \mathbf{Z}, \mathbf{W}) \propto L(\mathbf{Z} | \boldsymbol{\eta}, \mathbf{v}) f(\boldsymbol{\eta} | \boldsymbol{\theta}, \mathbf{W}) f(\mathbf{v} | \sigma_d) f(\boldsymbol{\theta}) f(\sigma_d), \tag{17}$$

where the likelihood function $L(\mathbf{Z} | \boldsymbol{\eta}, \mathbf{v})$ is

$$L(\mathbf{Z} | \boldsymbol{\eta}, \mathbf{v}) \propto \prod_{j=1}^{n} \left(\frac{\exp(\lambda_j)}{1 + \exp(\lambda_j)} \right)^{Z(\mathbf{s}_j)} \left(\frac{1}{1 + \exp(\lambda_j)} \right)^{1 - Z(\mathbf{s}_j)},$$

with λ_j being the jth element of $\boldsymbol{\lambda} = \boldsymbol{\mu} + \mathbf{K}_y \boldsymbol{\eta} + \boldsymbol{\delta}$, and $f(\boldsymbol{\eta} | \boldsymbol{\theta}, \mathbf{W})$ and $f(\mathbf{v} | \sigma_d)$ are

$$f(\boldsymbol{\eta} | \boldsymbol{\theta}, \mathbf{W}) \propto \prod_{k=1}^{J_y} \frac{1}{\sigma_{\eta,k}(\boldsymbol{\theta})} \exp\left(-\frac{(\eta_k - \mu_{\eta,k}(\boldsymbol{\theta}))^2}{2\sigma_{\eta,k}(\boldsymbol{\theta})^2} \right),$$

$$f(\mathbf{v} | \sigma_d) \propto \prod_{l=1}^{J_d} \frac{1}{\sigma_d} \exp\left(-\frac{v_l^2}{2\sigma_d^2} \right),$$

where $\mu_{\eta,k}(\boldsymbol{\theta})$ and $\sigma_{\eta,k}^2(\boldsymbol{\theta})$ are the mean and the variance of the kth element of $\boldsymbol{\eta}(\boldsymbol{\theta}, \mathbf{W})$, v_l is the lth element of $\mathbf{v}$, and σ_d^2 is the common variance for $v_1 \ldots v_{J_d}$. For the priors we assume that $f(\boldsymbol{\theta})$ is a d-dimensional uniform density whose support covers all plausible values of $\boldsymbol{\theta}$ and $f(\sigma_d)$ is an inverse-Gamma density with the shape parameter a_d and the scale parameter b_d. The functions $L(\mathbf{Z}|\boldsymbol{\eta}, \mathbf{v})$, $f(\boldsymbol{\eta}|\boldsymbol{\theta}, \mathbf{W})$, and $f(\mathbf{v}|\sigma_d)$ are based on proper densities, hence the posterior is proper as long as the priors $f(\boldsymbol{\theta})$ and $f(\sigma_d)$ are proper. The observations $Z(\mathbf{s}_1), \ldots, Z(\mathbf{s}_n)$ are conditionally independent given the values of the random coefficients $\boldsymbol{\eta}$ and $\mathbf{v}$ and the dependence between them is accounted for through the basis matrices $\mathbf{K}_y$ and $\mathbf{K}_d$. Based on the specifed posterior one can infer the parameters via MCMC.

Finding the basis $\mathbf{K}_d$ that can precisely represent the discrepancy process with a small number of basis vectors is important for computational tractability. To this end, we use the following procedure that is inspired by the definition of the discrepancy term:

1. For each location $\mathbf{s}_j$, compute the signed proportion of mismatch between the model output and the observational data as $r_j = \sum_{i=1}^p \mathrm{sgn}(Y(\boldsymbol{\theta}_i, \mathbf{s}_j) - Z(\mathbf{s}_j))I(Y(\boldsymbol{\theta}_i, \mathbf{s}_j) \neq Z(\mathbf{s}_j))/p$ where sgn is the sign function.

2. Set $J_d = 1$ and hence $\mathbf{K}_d$ is reduced to a n-dimensional vector $\mathbf{k}_d$. Define the jth element of $\mathbf{k}_d$ as $\log(\frac{1+r_j}{1-r_j})$ if $|r_j| > c$, or as 0 if $|r_j| < c$. The random coefficient vector $\mathbf{v}$ is also reduced to a univariate random variable $v \sim N(0, \sigma_d^2)$.

The goal of step 1 is to capture a common discrepancy pattern that is persistent across all parameter settings. For this procedure to work the design points $\boldsymbol{\theta}_1, \ldots, \boldsymbol{\theta}_p$ have to be a representative sample of plausible values of $\boldsymbol{\theta}$, and we expect that this holds for the Latin hypercube design that we are using here. In step 2 we apply logit transformation $\log\left(\frac{1+r_j}{1-r_j}\right)$ for $-1 \leq r_j \leq 1$ to translate the identified discrepancy pattern into logit scale since the discrepancy term $\mathbf{k}_d v$ needs to be specified for the natural parameters. Note that the cut-off value c in step 2 needs to be determined a priori. Choosing a value of c that is too large results in loss of important discrepancy patterns in $\mathbf{k}_d$ and, on the other hand, a value of c that is too small causes identifiability issues in estimating $\boldsymbol{\theta}$. In the simulated examples described in Section 5.1, we have found that the value of $c = 0.5$ strikes a nice balance, and yields a discrepancy basis that capture the true simulated discrepancy patterns reasonably well (See Figure A1 in the supplement). This value of c is a heuristic but it appears to work well for the variety of examples to which we have applied our methods. We set $c = 0.5$ for the remainder of this

paper. Note also that $\log(\frac{1+r_j}{1-r_j})$ can take a positive or negative infinite when $r_j = 1$ or $r_j = -1$. To prevent this, we set $r_j = 0.999 \times \text{sgn}(r_j)$, where $\text{sgn}(r_j)$ is the sign of r_j, when computing $\log(\frac{1+r_j}{1-r_j})$ if $|r_j|$ is greater than 0.999.

4.4 Procedure Summary

Let $\mathbf{Y}$ be an $n \times p$ matrix of the computer model output where the columns represent different spatial locations and the rows represent different parameter settings and $\mathbf{Z}$ denotes an n-dimensional vector of observational data (defined in Section 3). We summarize the overall emulation-calibration procedure described in this section as follows:

1. Dimension-reduction of computer model output: Compute logistic principal components of $\mathbf{Y}$ to reduce the dimensionality from n to J_y (details in Section 4.1) by maximizing the likelihood function in (7). We store the principal component scores in a $p \times J_y$ matrix $\mathbf{W}$, the principal component basis in an $n \times J_y$ matrix $\mathbf{K}_y$, and the location means in an n-dimensional vector $\boldsymbol{\mu}$ (see (6) for their definition).

2. Gaussian process-based univariate emulators: We construct a one-dimensional Gaussian process emulator for each column of $\mathbf{W}$ (details in Section 4.2) with the covariance function in (14). Denote the J_y-dimensional vector of the emulated principal components at a new parameter value $\boldsymbol{\theta}$ by $\boldsymbol{\eta}(\boldsymbol{\theta}, \mathbf{W})$.

3. Constructing a discrepancy basis: Find the discrepancy basis vector $\mathbf{k}_d$ by comparing each row of $\mathbf{Y}$ and $\mathbf{Z}$ (details in Section 4.3). Denote the coefficient for the discrepancy basis vector by v.

4. Calibration using Markov chain Monte Carlo: Based on the posterior density in (17) infer the input parameters $\boldsymbol{\theta}$, the principal components $\boldsymbol{\eta}$, the discrepancy coefficient v, and the discrepancy variance σ_d^2 using the Metropolis-Hastings algorithm (details in Section 4.3).

Our procedure requires estimating only $J_y + d + 2$ parameters in the calibration step. For our ice sheet model calibration problem, this corresponds to only $10 + 10 + 2 = 22$ parameters. Note that it would require estimating $n + d + 1 = 3,182 + 10 + 1 = 3,193$ parameters without dimension reduction.

5 Implementation Details and Results

In this section we study the application of our approach to simulated examples and then calibrate the PSU3D-ICE model based on the real observational data. We provide descriptions for each of the calibrated parameters as well as scientific interpretations of our results.

5.1 Simulated Examples

We now provide a discussion of our investigation of our approach in the context of simulated examples. We describe our construction of simulated examples and results from the applications of our methods to these examples, along with implementation details for our method. We apply our method to (i) a simple synthetic ice sheet model example to study the properties of our method, and to (ii) the PSU3D-ICE to estimate the input parameters of the model and make projections for future ice sheet volume changes in the Amundsen basin region.

Simple Numerical Example. We begin with a simple numerical example. Unlike the real ice sheet model calibration problem, this example does not have complicating issues such as lack of identifiability of input parameters or sparsity of design points in the parameter space, and hence it provides a nice first test for our calibration methods.

We defined the model output as $Y(\boldsymbol{\theta}, \mathbf{s}) = I(U(\boldsymbol{\theta}, \mathbf{s}))$ where

$$U(\boldsymbol{\theta}, \mathbf{s}) = \sqrt{1 - s_1^2 - \left(\frac{s_2}{1.5}\right)^2 - \theta_1 + \theta_2(s_2 + 1.5)},$$

with $\mathbf{s} = (s_1, s_2)$ and $\boldsymbol{\theta} = (\theta_1, \theta_2)$ for $0.3 < \theta_1 < 0.65$, $0 < \theta_2 < 0.2$, $0 < s_1 < 1$, and $-1.5 < s_2 < 1.5$. We form an ensemble of model outputs with 100 runs where the design points for (θ_1, θ_2) are on a regular 10×10 lattice covering the entire parameter space $\boldsymbol{\Theta} = [0.3, 0.65] \times [0, 0.2]$. Each model run $\mathbf{Y}(\boldsymbol{\theta}_i)$ is a spatial pattern on a 30×30 regular lattice that covers the entire spatial field $\mathcal{S} = [-1, 1] \times [-1.5, 1.5]$ and hence $n = 900$. See Figure A2 in the Supplement for 16 sample model runs. The first parameter θ_1 controls the overall size of the grey area and the second parameter θ_2 changes both the shape and the size of the grey area. We set the number of principal components to $J_y = 10$ based on leave-10-percent-out cross-validation; using more than 10 principal components does not significantly improve the emulation performance in our cross-validation experiments. The overall misclassification rate is less than 5%. We construct a synthetic observational data set by choosing the model run with $(\theta_1, \theta_2) = (0.494, 0.089)$ as

18

the synthetic truth and contaminating the corresponding model output with noise generated from the discrepancy process, defined as a zero-mean Gaussian process with an exponential covariance function with the partial sill of 1.5, the range of 0.03 and the nugget of 0.00001. This affects the resulting binary pattern considerably by changing roughly 10% of the original output. We repeat the same experiment with 10 different realizations from the discrepancy process and the results are summarized in Figure A3 in the Supplement. The results show that, on average, we can recover the true input parameter setting reasonably well in this simple numerical setting.

Realistic Example Using the Ice Sheet Model PSU3D-ICE. We now work with a more realistic synthetic observational data set to verify that our calibration approach works well in the context of the real ice sheet model calibration problem. Here we use the model runs from the PSU3D-ICE model described in Section 2 to generate the example. This estimation problem is more challenging than the example described in the previous section because it involves complicated interactions between the input parameters. Also, the input parameter settings are much more sparsely distributed in the parameter space (499 ensemble members in 10 dimensional space), which potentially makes emulation, as well as calibration, more difficult.

We select model run #394 as the synthetic truth, because it is among the model runs closest to the observational data. We count the number of pixels where the observational data and the model output have the same value, i.e. we compute $\sum_{j=1}^{n} I(Z(\mathbf{s}_j) = Y(\boldsymbol{\theta}_i, \mathbf{s}_j))$ for each $\boldsymbol{\theta}_i$ where $I(.)$ is the indicator function. A model run is close to the observations if this count is large. Since in reality the model-observation discrepancy operates in terms of the actual ice thickness patterns (the binary ice-no ice patterns are derived from these data), we construct the discrepancy pattern in terms of ice thickness and translate it into a binary spatial pattern. We use the following steps to construct a realistic model-observation discrepancy.

1. By comparing the original model runs and the observational data that are spatial patterns of ice thickness, find the top 60% model runs with the smallest root mean squared error (RMSE) values.

2. For each spatial location, take the average of the difference between the observational data and the model runs selected in step 1 to find the common discrepancy pattern in ice thickness.

3. Subtract common discrepancy pattern found in step 2 from the ice thickness output corresponding to the synthetic truth. The resulting pattern is synthetic observational data for ice thickness.

4. Dichotomize the ice thickness pattern computed in step 3 at 0 to obtain synthetic observational data for ice-no ice pattern.

The procedure described in Section 4.3 recovers the superimposed discrepancy reasonably well (Figure A1 in the Supplement, lower panels).

We choose to use 10 principal components for dimension reduction based on the same cross-validation criteria described in the previous section. The leave-10-percent-out cross-validation confirms that our emulator can predict the model output precisely (Figure 2), with an overall error rate of 4%. To translate the probabilities $p_1(\boldsymbol{\theta}), \ldots, p_n(\boldsymbol{\theta})$ from our emulator into predictions for the binary outcome, we simply dichotomize them using 0.5 as a threshold. We give a non-informative prior $IG(2,3)$ to σ_d^2 and flat priors to the input parameters in $\boldsymbol{\theta}$. The range of each flat prior is restricted to the range for the design points $\boldsymbol{\theta}_1, \ldots, \boldsymbol{\theta}_p$. Using the standard Metropolis-Hastings algorithm we generate MCMC sample for $\boldsymbol{\theta}$ while integrating out $\boldsymbol{\eta}$, v, and σ_d^2. For each experiment we obtain MCMC chain with 1,000,000 iterations. Looking at MCMC standard errors (Jones et al., 2006; Flegal et al., 2008) suggests that the sample size was large enough to estimate posterior means while accounting for autocorrelations. We also overlaid the marginal density plots obtained after half the run over the marginal density plots obtained after the entire run, confirming that the plots do not show significant changes and the results are therefore stable. The computation takes about 120 hours for the entire MCMC run on a system with Intel Xeon E5450 Quad-Core 3.0 GHz..

The pairwise joint densities of input parameters are shown in Figure 3. Since the scientific interest is mainly in the four parameters, ocean sub-ice-shelf melt factor (OCFAC), calving factor (CALV), basal sliding coefficient (CRH), and asthenospheric relaxation e-folding time (TAU), we display the results for only these parameters (see Section 5.2 below for the reason). The density plots indicate that the marginal posterior densities for the first three densities peak around the true parameter values, but the marginal densities for TAU do not recover the true values and show large dispersion comparing to the other parameters. We hypothesize that the binary spatial patterns are not informative about TAU. The probable reason for parameter TAU not being well constrained is that the statistical analysis above is limited to calibration with the

modern observed ice state. TAU is the *e*-folding time scale of asthenospheric relaxation below the varying ice load (see Table 1 and Section 5.2 below), and its primary effect on ice evolution occurs during the main deglacial retreat phase, 12 to 8 ka. The ice retreat is nearly complete by 8 ka in most of our model runs, leaving ample time for the asthenosphere to relax towards the modern state, regardless of the exact value of TAU. Calibration and statistical techniques using past grounding-line positions vs. those estimated from geologic data over the last 15 kyr (Larter et al., 2014) will likely be able to diagnose and constrain this important parameter.

Using the MCMC chain for the input parameters, we generate projections for WAIS volume change. Here we present projection results for 500 and 1000 years from the present day. We build an emulator for ice volume changes generated from the PSU3D-ICE and convert the MCMC chain for input parameters into projections using the emulator. The results in Figure 4 show the predictive distribution of the ice volume change projections corresponding to the estimated posterior density. For comparison, we have also computed the predictive density by assuming that all the parameter settings in the model ensemble are equally likely. We compare these densities with the assumed true ice volume change projection values produced by the parameter settings for the synthetic truth. For both time points (500 and 1000 years from the present) the 95% prediction intervals cover the synthetic true ice volume change projections. The mode of the predictive density matches well with the true ice volume change projection for 500 years, but the mode for the ice volume change for 1000 years does not match with the assumed true value. We hypothesize that this is due to the large uncertainty for TAU, which controls the long term ice sheet behavior. We provide a longer discussion of this in the next section.

5.2 Calibration of PSU3D-ICE Using Observational Data

We now calibrate PSU3D-ICE using the observational data. The calibration results based on the observations from the Bedmap2 dataset (Fretwell et al., 2013) are shown in Figure 6 and 7.

Parameter Description. Out of the 10 ice-sheet model parameters that were varied and inferred we focus on four important parameters. These parameters are highly uncertain even though they have strong effects on model behavior. Most parameters and inputs that concern interior grounded-ice processes, inland of the modern grounding zone, are relatively well known, based on modern data and well established in previous model-data studies. Examples are

ice rheology, surface accumulation, and basal sliding through inverse procedures. However, processes that affect the floating ice shelves, and also properties of past grounded ice that advanced out over the Antarctic continental shelf at glacial maxima, are much less well known, and we focus on important parameters in this category. The 4 parameters and processes are:

- Ocean sub-ice-shelf melt factor (OCFAC): Oceanic melting at the base of floating ice shelves, due to warm waters flowing from the open ocean into the cavities below the ice shelves. This affects ice shelf thickness, and changes buttressing of interior ice. Recent increases in ocean melt rates are considered to be the main cause of drastic ongoing ice retreat in the ASE sector of WAIS (Pritchard et al., 2012; Rignot and Jacobs, 2002). For small (large) OCFAC values, oceanic melting is reduced (increased), ice shelves thicken (thin), discharge of interior ice across the grounding line decreases (increases), and grounding lines tend to advance (retreat).

- Calving factor (CALV): Calving of icebergs at the oceanic edge of floating shelves. This process is not well understood, probably depending on pre-existing fracture regimes, large-scale stresses, and hydrologic conditions, yet has important effects on ice-shelf extent and feedback on buttressing and internal ice, both for the modern state and also for past and future variations. There is little consensus on calving parameterizations. We use a common approach based on (highly parameterized) crevasse depths and their ratio to ice thickness (Benn et al. 2007; Nick et al., 2010). For small (large) CALV, calving is decreased (increased), producing more (less) extensive floating shelves, and greater (lesser) buttressing of interior ice.

- Basal sliding coefficient (CRH): Basal sliding of grounded ice at the interface with bedrock. For beds at the ice pressure-melt point, for a given driving stress, sliding depends mainly on whether the bed is hard and non-deformable (crystalline rock, sticky, slow sliding) or soft and deformable (unconsolidated sediment or till, slippery, fast sliding). The coefficient values in the basal sliding law relating basal stress to velocity have strong effects on the overall ice profile shape and thicknesses, and affect the overall sensitivity to climate change. Coefficients under modern grounded ice are deduced by inverse methods (Pollard and DeConto, 2012a; Morlighem et al., 2013), but they are relatively unconstrained for modern oceanic beds, where grounded ice advanced during the last glacial maximum 20 to 15 ka. Most oceanic areas around Antarctica are covered in deformable sediment today,

due to marine sedimentation and to generation and transport by previous ice advances. For these regions, there is a wide plausible range of relatively large sliding coefficients that have significant effects on model results. Here, we vary the sliding coefficient CRH just for modern oceanic areas.

- Asthenospheric relaxation e-folding time (TAU): The ice sheet evolution on 10^3 year timescales depends strongly on the bedrock response to varying ice load. During deglacial retreat, the bedrock rebounds upwards due to the retreating ice load, but with an $O(10^3)$ year lag, and this lag has an important positive feedback via deeper bedrock and grounding-line depths. As in many ice models, this bedrock response is represented by a simple Earth model consisting of an elastic plate (lithosphere) over a local e-folding lagged relaxation towards isostatic equilibrium (asthenosphere). Based on more sophisticated Earth models, the asthenospheric e-folding time scale is commonly set to 3 kyr (e.g., Gomez et al., 2013), but note that recent studies suggest considerably shorter time scales for some West Antarctic regions (Whitehouse et al., 2012a).

Results. The estimated discrepancy pattern by the procedure described in Section 4.3 is shown in Figure 5. Much of the discrepancy pattern in Figure 5 is due to a known shortcoming of the ice model that tends to fill narrow bays and passages between mainland and nearby islands with grounded ice, where there is only floating ice in the real world. This is partly due to the coarse model grid size (20 km) not sufficiently resolving the passages, and also presumably due to the lack of fine-scale variations in oceanic basal melting that could well exist in these passages due to local ocean currents.

As seen in the pairwise density plots in Figure 6, the best values of ocean melt coefficient (OCFAC) and calving factor (CALV) are roughly in their mid-range, i.e., quite close to the values in the nominal model that relied on prior tuning by the model developers (Pollard and DeConto, 2012a). There is a slight indication that OCFAC should be somewhat smaller than the value found by Pollard and DeConto (2012a). The best CALV value, 0.5, corresponds to an unchanged nominal value.

The bedrock (asthenospheric) e-folding rebound time TAU is not constrained well in Figure 6. Although the uppermost values (corresponding to 6 to 7 kyr in the original scale) are excluded, values below 6 kyr have similar probabilities. As discussed above, this is expected because TAU primarily affects past ice distribution during deglaciation, with little effect on

modern ice. There is a slight tendency to favor small TAU (less than 0.2, corresponding to less than 2 kyr), compared to the nominal prior value of 3 kyr (Pollard and DeConto, 2012a), but this is a weak tendency.

There is one strong signal in Figure 6: the best-fit basal sliding coefficient CRH for continental-shelf (modern ocean) regions, is found to be quite high, 0.8, corresponding to 10^{-6} m a^{-1} P a^{-2}. The narrowing of the uncertainty for CRH is valuable information for models. Even though the validation here is based only on results for the modern ice sheet (for which there is no direct effect of CRH if the results are realistic, because all modern ice should be floating in the affected regions), CRH still has a significant influence on the modern state by affecting ice profiles during the recent evolution over the last few thousand years. The relatively high (slippery) value of 10^{-6} is consistent with geologic data at LGM, indicating that grounded ice thicknesses across the modern Ross Sea Embayment were relatively thin at LGM (deduced from geologic data in the Transantarctic Mountains and other outcrops; Ackert Jr. et al., 2013; Anderson et al., 2013).

In the ice-volume change projections for 500 and 1000 years from present (Figure 7), the left-hand tail of lower ice volumes may seem counter-intuitive, given the imposed climatic warming after year 0 (present day). This tail is probably due to a subset of highly unrealistic runs, whose grounding lines retreat drastically inland beyond the modern coastline much too early, 100's to 1000's years before present, and then re-advance due to the lagged bedrock rebound (discussed above), producing modern grounding lines close to observed despite very unrealistic past behavior. This likely happens in runs with the longest TAU time-scale values, 7 kyrs. As mentioned above, calibration based on past geologic data would reduce this tail.

The difference between the mode at 1000 years from present and the assumed-true value (Figure 4) could well be due to the unconstrained TAU values in Figure 3 and 6. As well as affecting past behavior, TAU also has an effect on long-term future retreat via the feedback on grounding-line depths discussed above. Nevertheless, the basic projection of drastic future retreat and a few meters (less than 10 meters) equivalent sea-level rise within the next 1000 years is a robust result, and occurs in nearly all runs with reasonably realistic past behavior. This is consistent with other recent studies of future ice-sheet retreat in the Amundsen Sea Embayment sector (Joughin et al., 2014; Rignot et al., 2014).

Caveats. Similar to other calibration frameworks, care is needed in specifying the model-

observation discrepancy to avoid identifiability issues. In our calibration approach specifying the discrepancy model requires a pre-determined tuning parameter c, which determines whether a specific pixel exhibits a persistent model-observation discrepancy (see Section 4.3). While our choice of $c = 0.5$ appears to be somewhat ad-hoc, we have verified through a detailed study of multiple simulated examples that this choice of c generally yields a discrepancy pattern that captures well the true discrepancy pattern. In addition to the simulated example (Section 5.1) and the PSU3D-ICE model used in this paper, we have applied our approach with c set to 0.5 in the context of a completely different ice sheet model (SICOPOLIS; Greve, 1997; Greve et al., 2011) and verified that the identified discrepancy is similar to the true discrepancy pattern used to create the simulated examples.

Our scientific conclusions are subject to the following usual caveats. It should be emphasized that the extensions of our runs beyond present are projections based only on a single, simplified greenhouse-gas scenario. Various greenhouse-gas scenarios for the future are available as Representative Concentration Pathways (RCPs Moss et al., 2010; Meinshausen et al., 2011), which can be used with climate models to provide forcing for the ice sheet model. However, the RCPs themselves range over a wide envelope (RCP 2.6, RCP 4.5, RCP 6.0, RCP 8.5) depending on future societal activity, from strong through intermediate mitigation to "business-as-usual". These scenarios should ideally also be treated as sources of additional projection uncertainty. This is a complex additional challenge and a potentially important direction for future work. In this preliminary study we limit the variable parameters to physical model attributes, and specify a relatively simple future climate warming. Note also that the volumes in Figures 4 and 7 are only for the WAIS domain of these nested model runs, not for all Antarctica (although the East Antarctic contribution is expected to be comparatively small; Pollard and DeConto, 2009).

Our calibration results are based only on the modern day grounding-line geometry and it might be possible to improve the results by using additional information such as the past grounding line positions. We expect that this will lead to a better constrained probability density of TAU. As we mentioned above, one future direction is to formulate a rigorous calibration approach that enables us to combine these multiple sources of information. In addition, we use only the grounding-line geometry and hence ignore the spatial patterns of floating ice (ice shelves) and the distribution of ice thickness. Incorporating these additional sources of information requires calibration using other types of non-Gaussian data such as bounded spatial

25

data with many zeros and spatial data with multinomial responses; this is beyond the scope of this paper. Also, methods combining calibration with other types of past geologic data will be challenging but necessary for comprehensive model validation (mainly Relative Sea Level records, GPS uplift rates, and cosmogenic age-elevation data; Briggs and Tarasov, 2013; Briggs et al., 2013, 2014; Whitehouse et al., 2012b,a).

6 Summary

We have formulated a novel computer model emulation and calibration approach for high-dimensional binary spatial data. We have applied our approach to calibrate a computer model that describes the dynamics of the West Antarctic ice sheet. The results of this calibration provide some understanding of the role of important parameters in the model, and also allow us to produce preliminary projections, with uncertainties, of future ice sheet volume change. Using a logistic principal component analysis and basis representation, we can efficiently handle high-dimensional binary spatial data; our dimension-reduced approach therefore addresses challenges in handling high-dimensional binary spatial data by removing the need to simulate underlying high-dimensional processes and avoiding computations with large matrices. The logistic principal component analysis is a special case of principal component analysis for the one parameter exponential family and can therefore be easily extended to other types of spatial data such as spatial count processes. Incorporating complicated model-observation discrepancies is a challenging problem in general. We allow for a flexible but computationally expedient model for discrepancy. Our study of simulated examples shows that our approach can estimate the input parameters reasonably well even in the presence of considerable, realistic model-observation discrepancies. The application of our methods to real ice sheet observational data allows us to characterize uncertainties in both our model parameter estimates as well as our projections for future ice volume change.

References

Robert P Ackert Jr., Aaron E Putnam, Sujoy Mukhopadhyay, David Pollard, Robert M DeConto, Mark D Kurz, and Harold W Borns Jr. Controls on interior west antarctic ice sheet elevations: inferences from geologic constraints and ice sheet modeling. *Quaternary Science Reviews*, 65:26–38, 2013.

Richard B Alley, John Thomas Andrews, Julia Brigham-Grette, G. K. C. Clarke, K. M. Cuffey, J. J. Fitzpatrick, S. Funder, S. J Marshall, G. H. Miller, J. X. Mitrovica, D.R. Muhs, B. L. Otto-Bliesner, L. Polyakk, and J.W.C. White. History of the greenland ice sheet: paleoclimatic insights. *Quaternary Science Reviews*, 29(15):1728–1756, 2010.

John B Anderson, Howard Conway, Philip J Bart, Alexandra E Witus, Sarah L Greenwood, Robert M McKay, Brenda L Hall, Robert P Ackert, Kathy Licht, Martin Jakobsson, and J. O. Stone. Ross Sea paleo-ice sheet drainage and deglacial history during and since the LGM. *Quaternary Science Reviews*, 100:31–54, 2013.

P.J. Applegate, N. Kirchner, E.J. Stone, K. Keller, and R. Greve. An assessment of key model parametric uncertainties in projections of Greenland Ice Sheet behavior. *The Cryosphere*, 6 (3):589–606, 2012.

M.J. Bayarri, J.O. Berger, J. Cafeo, G. Garcia-Donato, F. Liu, J. Palomo, R.J. Parthasarathy, R. Paulo, J. Sacks, and D. Walsh. Computer model validation with functional output. *The Annals of Statistics*, 35(5):1874–1906, 2007.

K.S. Bhat, M. Haran, and M. Goes. Computer model calibration with multivariate spatial output: A case study. In M.H. Chen, P. Müller, D. Sun, K. Ye, and D.K. Dey, editors,

Frontiers of Statistical Decision Making and Bayesian Analysis, pages 168–184. Springer, 2010.

K.S. Bhat, M. Haran, R. Olson, and K. Keller. Inferring likelihoods and climate system characteristics from climate models and multiple tracers. *Environmetrics*, 23(4):345–362, 2012.

Robert A Bindschadler, Sophie Nowicki, Ayako Abe-Ouchi, Andy Aschwanden, Hyeungu Choi, Jim Fastook, Glen Granzow, Ralf Greve, Gail Gutowski, Ute Herzfeld, Charles Jackson, Jesse Johnson, Constantine Khroulev, Anders Levermann, William H. Lipscomb, Maria A. Martin, Mathieu Morlighem, Byron R. Parizek, David Pollard, Stephen F. Price, Diandong Ren, Fuyuki Saito, Tatsuru Sato, Hakime Seddik, Helene Seroussi, Kunio Takahashi, Ryan Walker, and Wei Li Wang. Ice-sheet model sensitivities to environmental forcing and their use in projecting future sea level (the searise project). *Journal of Glaciology*, 59(214):195–224, 2013.

R Briggs, D Pollard, and L Tarasov. A glacial systems model configured for large ensemble analysis of Antarctic deglaciation. *The Cryosphere Discussions*, 7(2):1533–1589, 2013.

R.D. Briggs and L. Tarasov. How to evaluate model-derived deglaciation chronologies: a case study using Antarctica. *Quaternary Science Reviews*, 63:109–127, 2013.

Robert D Briggs, David Pollard, and Lev Tarasov. A data-constrained large ensemble analysis of Antarctic evolution since the Eemian. *Quaternary Science Reviews*, 103:91–115, 2014.

Rob Carnell. *lhs: Latin Hypercube Samples*, 2012. URL `http://CRAN.R-project.org/package=lhs`. R package version 0.10.

W. Chang, P. Applegate, H. Haran, and K. Keller. Probabilistic calibration of a greenland ice sheet model using spatially-resolved synthetic observations: toward projections of ice mass loss with uncertainties. *Geoscientific Model Development*, 7:1933–1943, 2014a.

Won Chang, Murali Haran, Roman Olson, and Klaus Keller. Fast dimension-reduced climate model calibration and the effect of data aggregation. *The Annals of Applied Statistics*, 8(2): 649–673, 2014b.

Won Chang, Murali Haran, Roman Olson, and Klaus Keller. A composite likelihood approach to computer model calibration using high-dimensional spatial data. *Statistica Sinica*, 25: 243–259, 2015.

Michael Collins, S. Dasgupta, and Robert E. Schapire. A generalization of principal components analysis to the exponential family. In T.G. Dietterich, S. Becker, and Z. Ghahramani, editors, *Advances in Neural Information Processing Systems 14*, pages 617–624. MIT Press, 2002.

Jan de Leeuw. Principal component analysis of binary data by iterated singular value decomposition. *Computational statistics & data analysis*, 50(1):21–39, 2006.

Pierre Deschamps, Nicolas Durand, Edouard Bard, Bruno Hamelin, Gilbert Camoin, Alexander L Thomas, Gideon M Henderson, Jun'ichi Okuno, and Yusuke Yokoyama. Ice-sheet collapse and sea-level rise at the Bølling warming 14,600 years ago. *Nature*, 483(7391):559–564, 2012.

J. M. Flegal, M. Haran, and G. L. Jones. Markov chain monte carlo: Can we trust the third significant figure? *Statistical Science*, 23(2):250–260, 2008.

P Fretwell, Hamish D Pritchard, David G Vaughan, J. L. Bamber, N. E. Barrand, R Bell, C Bianchi, R. G. Bingham, D. D. Blankenship, G Casassa, G. Catania, D. Callens, H. Conway, A.J. Cook, H.F.J. Corr, D. Damaske, V. Damm, F. Ferraccioli, R. Forsberg, S. Fujita, Y. Gim, P. Gogineni, J.A. Griggs, R.C.A. Hindmarsh, P. Holmlund, J.W. Holt, R.W. Jacobel, A. Jenkins, W. Jokat, T. Jordan, E.C. King, J. Kohler, W. Krabill, M. Riger-Kusk, K.A. Langley, G. Leitchenkov, C. Leuschen, B.P. Luyendyk, K. Matsuoka, J. Mouginot, F.O. Nitsche, Y. Nogi, O.A. Nost, S.V. Popov, E. Rignot, D.M. Rippin, A. Rivera, J. Roberts, N. Ross, M.J. Siegert, A.M. Smith, D. Steinhage, M. Studinger, B. Sun, B.K. Tinto, B.C. Welch, D. Wilson, D.A. Young, C. Xiangbin, and A. Zirizzotti. Bedmap2: improved ice bed, surface and thickness datasets for antarctica. *The Cryosphere*, 7(1):375–393, 2013.

Rupert M Gladstone, Victoria Lee, Jonathan Rougier, Antony J Payne, Hartmut Hellmer, Anne Le Brocq, Andrew Shepherd, Tamsin L Edwards, Jonathan Gregory, and Stephen L Cornford. Calibrated prediction of pine island glacier retreat during the 21st and 22nd centuries with a coupled flowline model. *Earth and Planetary Science Letters*, 333:191–199, 2012.

Natalya Gomez, David Pollard, and Jerry X Mitrovica. A 3-d coupled ice sheet–sea level model applied to antarctica through the last 40 ky. *Earth and Planetary Science Letters*, 384:88–99, 2013.

Ralf Greve. Application of a polythermal three-dimensional ice sheet model to the greenland

ice sheet: response to steady-state and transient climate scenarios. *Journal of Climate*, 10 (5):901–918, 1997.

Ralf Greve, Fuyuki Saito, and Ayako Abe-Ouchi. Initial results of the searise numerical experiments with the models sicopolis and icies for the greenland ice sheet. *Annals of Glaciology*, 52(58):23–30, 2011.

D. Higdon, J. Gattiker, B. Williams, and M. Rightley. Computer model calibration using high-dimensional output. *Journal of the American Statistical Association*, 103(482):570–583, 2008.

David R Hunter and Kenneth Lange. A tutorial on mm algorithms. *The American Statistician*, 58(1):30–37, 2004.

G. Jones, M. Haran, B. S. Caffo, and R. Neath. Fixed-width output analysis for markov chain monte carlo. *Journal of the American Statistical Association*, 101(476):1537–1547, 2006.

V Roshan Joseph and Ying Hung. Orthogonal-maximin latin hypercube designs. *Statistica Sinica*, 18(1):171, 2008.

Ian Joughin, Benjamin E Smith, and Brooke Medley. Marine ice sheet collapse potentially under way for the thwaites glacier basin, west antarctica. *Science*, 344(6185):735–738, 2014.

M.C. Kennedy and A. O'Hagan. Bayesian calibration of computer models. *Journal of the Royal Statistical Society. Series B (Statistical Methodology)*, 63(3):425–464, 2001.

Nina Kirchner, Kolumban Hutter, Martin Jakobsson, and Richard Gyllencreutz. Capabilities and limitations of numerical ice sheet models: a discussion for Earth-scientists and modelers. *Quaternary Science Reviews*, 30(25):3691–3704, 2011.

Kenneth Lange, David R Hunter, and Ilsoon Yang. Optimization transfer using surrogate objective functions. *Journal of Computational and Graphical Statistics*, 9(1):1–20, 2000.

R.D. Larter, J.B Anderson, A.G.C Graham, K. Gohl, C.-D. Hillenbrand, M. Jakobsson, J.S Johnson, G. Kuhn, F.O. Nitsche, J.A. Smith, A.E. Witus, M.J. Bentley, J.A. Dowdeswell, W. Ehrmann, J.P. Klages, J. Lindow, C. Ó Cofaigh, and C. Spiegel. Reconstruction of changes in the Amundsen Sea and Bellingshausen Sea sector of the West Antarctic Ice Sheet since the Last Glacial Maximum. *Quarterly Scientific Review*, 100:55–86, 2014.

Le Brocq, A.M. and Payne, A.J. and Vieli, A. An improved Antarctic dataset for high resolution numerical ice sheet models (ALBMAP v1). *Earth System Science Data*, 2:247–260, 2010.

S. Lee, J. Z. Huang, and J. Hu. Sparse logistic principal components analysis for binary data. *The Annals of Applied Statistics*, 4(3):1579–1601, 2010.

Robert Lempert, Ryan L Sriver, and Klaus Keller. *Characterizing Uncertain Sea Level Rise Projections to Support Investment Decisions.* California Energy Commission, Publication Number: CEC-500-2012-056, 2012.

Christopher M Little, Michael Oppenheimer, Richard B Alley, Venkatramani Balaji, Garry KC Clarke, Thomas L Delworth, Robert Hallberg, David M Holland, Christina L Hulbe, Stan Jacobs, J. V. Johnson, H. Levy, W. H. Lipscomb, S. J. Marshall, B. R. Parizek, A. J. Payne, G. A. Schmidt, R. J. Stouffer, D. G. Vaughan, and M. Winton. Toward a new generation of ice sheet models. *Eos, Transactions American Geophysical Union*, 88(52):578–579, 2007.

F. Liu, MJ Bayarri, and JO Berger. Modularization in bayesian analysis, with emphasis on analysis of computer models. *Bayesian Analysis*, 4(1):119–150, 2009a.

Z Liu, BL Otto-Bliesner, F He, EC Brady, R Tomas, PU Clark, AE Carlson, J Lynch-Stieglitz, W Curry, E Brook, D. Erickson, R. Jacob, J. Kutzbach, and J. Cheng. Transient simulation of last deglaciation with a new mechanism for bølling-allerød warming. *Science*, 325(5938): 310–314, 2009b.

Michael D McKay, Richard J Beckman, and William J Conover. Comparison of three methods for selecting values of input variables in the analysis of output from a computer code. *Technometrics*, 21(2):239–245, 1979.

DJ McNeall, PG Challenor, JR Gattiker, and EJ Stone. The potential of an observational data set for calibration of a computationally expensive computer model. *Geoscientific Model Development*, 6(5):1715–1728, 2013.

Malte Meinshausen, Steven J Smith, K Calvin, John S Daniel, MLT Kainuma, JF Lamarque, K Matsumoto, SA Montzka, SCB Raper, K Riahi, et al. The rcp greenhouse gas concentrations and their extensions from 1765 to 2300. *Climatic Change*, 109(1-2):213–241, 2011.

M Morlighem, H Seroussi, E Larour, and E Rignot. Inversion of basal friction in Antarctica

using exact and incomplete adjoints of a higher-order model. *Journal of Geophysical Research: Earth Surface*, 118(3):1746–1753, 2013.

Richard H Moss, Jae A Edmonds, Kathy A Hibbard, Martin R Manning, Steven K Rose, Detlef P Van Vuuren, Timothy R Carter, Seita Emori, Mikiko Kainuma, Tom Kram, G. A Meehl, J. F. B. Mitchell, M. Nakicenovic., K. Riahi, Steven J. Smith, Ronald J. Stoufferand, Allison M. Thomson, John P. Weyant, and Thomas J. Wilbanks. The next generation of scenarios for climate change research and assessment. *Nature*, 463(7282):747–756, 2010.

Robert J Nicholls, Richard SJ Tol, and Athanasios T Vafeidis. Global estimates of the impact of a collapse of the west antarctic ice sheet: an application of fund. *Climatic Change*, 91(1-2):171–191, 2008.

W.R. Peltier. Global glacial isostacy and the surface of the ice-age Earth: The ICE-5G (VM2) model and GRACE. *Annual Review of Earth and Planetary Sciences*, 32:111–149, 2004.

D Pollard and R. M. DeConto. Description of a hybrid ice sheet-shelf model, and application to Antarctica. *Geoscientific Model Development*, 5:1273–1295, 2012a.

D Pollard and R. M. DeConto. A simple inverse method for the distribution of basal sliding coefficients under ice sheets, applied to Antarctica. *The Cryosphere Discussions*, 6(2):1405–1444, 2012b.

D. Pollard, R. M. DeConto, and R. B. Alley. Potential Antarctic Ice Sheet retreat driven by hydrofracturing and ice cliff failure. *Earth and Planetary Science Letters*, 2015. in press.

David Pollard and Robert M DeConto. Modelling West Antarctic ice sheet growth and collapse through the past five million years. *Nature*, 458(7236):329–332, 2009.

H. D. Pritchard, S. R. M. Ligtenberg, H. A. Fricker, D. G. Vaughan, M. R. Van den Broeke, and L Padman. Antarctic ice-sheet loss driven by basal melting of ice shelves. *Nature*, 484(7395):502–505, 2012.

Friedrich Pukelsheim. The three sigma rule. *The American Statistician*, 48(2):88–91, 1994.

E Rignot, J Mouginot, M Morlighem, H Seroussi, and B Scheuchl. Widespread, rapid grounding line retreat of pine island, thwaites, smith, and kohler glaciers, west antarctica, from 1992 to 2011. *Geophysical Research Letters*, 41(10):3502–3509, 2014.

Eric Rignot and Stanley S Jacobs. Rapid bottom melting widespread near Antarctic ice sheet grounding lines. *Science*, 296(5575):2020–2023, 2002.

J. Rougier. Comment on article by Sansó et al. *Bayesian Analysis*, 3(1):45–56, 2008.

J. Sacks, W.J. Welch, T.J. Mitchell, and H.P. Wynn. Design and analysis of computer experiments. *Statistical Science*, 4(4):409–423, 1989.

Mark C Serreze and Roger G Barry. Processes and impacts of arctic amplification: A research synthesis. *Global and Planetary Change*, 77(1):85–96, 2011.

Michael Stein. Large sample properties of simulations using Latin hypercube sampling. *Technometrics*, 29(2):143–151, 1987.

E.J. Stone, D.J. Lunt, I.C. Rutt, and E. Hanna. Investigating the sensitivity of numerical model simulations of the modern state of the greenland ice-sheet and its future response to climate change. *The Cryosphere*, 4(3):397–417, 2010.

P. L. Whitehouse, M. J. Bentley, G. A. Milne, M. A. King, and I. D. Thomas. A new glacial isostatic model for Antarctica: calibrated and tested using observations of relative sea-level change and present-day uplifts. *Geophysical Journal International*, 190:1464–1482, 2012a.

P.L. Whitehouse, M.J. Bentley, and A.M. Le Brocq. A deglacial model for Antarctica: geological constraints and glaciological modeling as a basis for a new model of Antarctic glacial isostatic adjustment. *Quarterly Scientific Review*, 32:1–24, 2012b.

Jinlun Zhang. Increasing antarctic sea ice under warming atmospheric and oceanic conditions. *Journal of Climate*, 20(11):2515–2529, 2007.

Parameter	Definition
OCFAC	Ocean sub-ice-shelf melt factor (.1 to 10) (non-dim). K in Eq. 17, PD12.
CALV	Calving factor (.316 to 3.16) (non-dim), multiplies combined crevasse depth to thickness ratio r in Eq. B7, PD15.
CRH	Basal sliding coeff. modern ocean bed (10^{-9} to 10^{-5}) (m yr^{-1} P a^{-2}) C in Eq. 11, PD12.
CRHASE	Extra multiplicative factor×CRH, inshore ASE (10^{-3} to 1) (non dim), multiplies C, only in inshore Amundsen Sea Embayment, Eq. 11, PD12.
TAU	Asthenospheric relaxation e-folding time scale= (1 to 6 kyr). τ in Eq. 33, PD12.
LITH	Lithospheric stiffness (10^{23} to 10^{25}) (N m). D in Eq. 30, PD12.
GEO	Geothermal heat flux (50 to 90) (mW m^{-2}). see section 2.7, PD12.
SUBPIN	Sub-grid ice-shelf pinning factor (0 to 4) (non-dim), multiplies s_{dev} in Eq. 13, PD12.
USCH	Grounding-line flux factor (0.5 to 5) (non-dim), multiplies q_g in Eq. 8, PD12.
LAPSE	γ (lower-case greek) in Eq. 34a, PD12. atmospheric lapse rate (-.005 to -.010) (°C m^{-1}).

Table 1: Ice-sheet model parameters varied in the LHC ensemble described in Section 2. The parameter ranges and units are shown in parentheses. The parameter values are uniformly spaced within each range, but for some variables, they are log-linear (i.e., the log of the parameter is varied uniformly), for OCFAC, CALV, CRH, CRHASE, LITH, and USCH. Parameters called "factors" are non-dimensional, multiplying existing terms. The corresponding symbols and equation numbers in Pollard and DeConto (2012a) and Pollard et al. (2015) called PD12 and PD15 respectively, are also shown in the table.

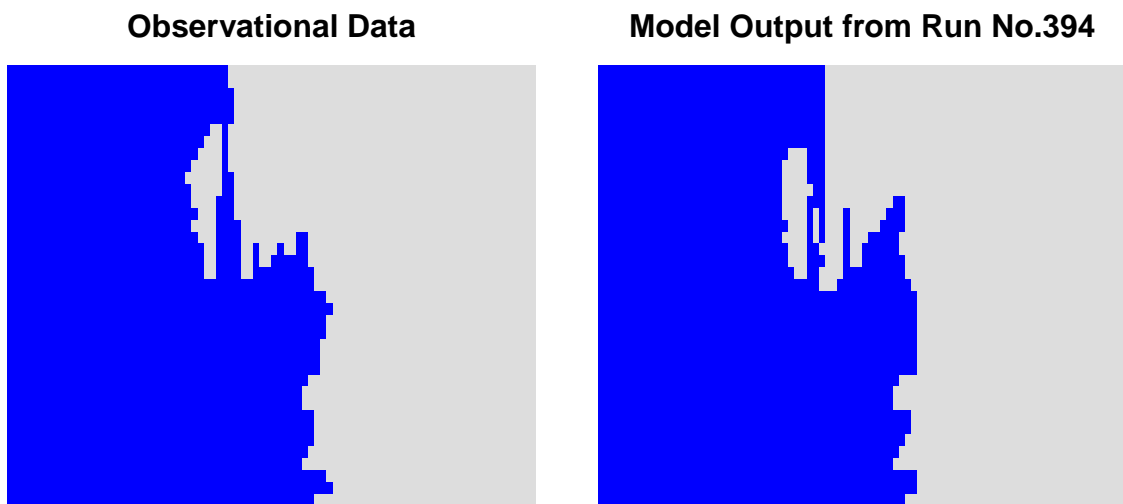**Observational Data**   **Model Output from Run No.394**

Figure 1: Spatial patterns of grounded ice from the observational dataset (Fretwell et al., 2013) (left) and an example PSU3D-ICE run (right). The gray pixels represent ice-covered locations. The model appears to be capable of reproducing observational patterns.
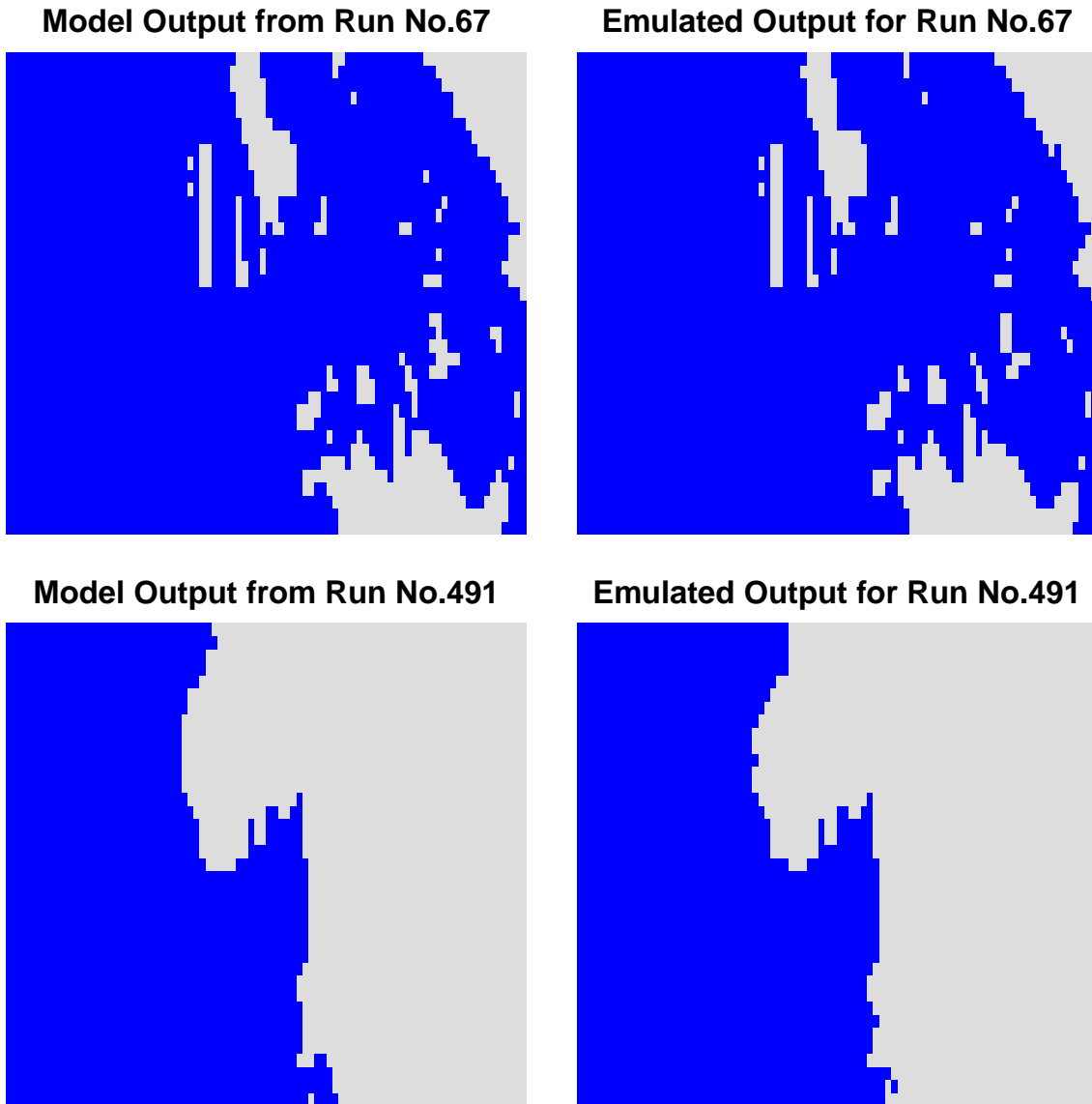
Model Output from Run No.67

Emulated Output for Run No.67

Model Output from Run No.491

Emulated Output for Run No.491

Figure 2: Two examples of leave-10-percent-out cross-validation results to study the performance of our logistic PCA based emulator. The gray pixels show ice-covered locations. (a) Comparison between the original (left) and the emulated (right) ice coverage patterns for model run no. 67. (b) The same comparison for model run no. 491. The graphical comparison shows that the emulated model output (right panel) approximates the original model output (left panel) fairly closely. Similar results hold for the other model runs.
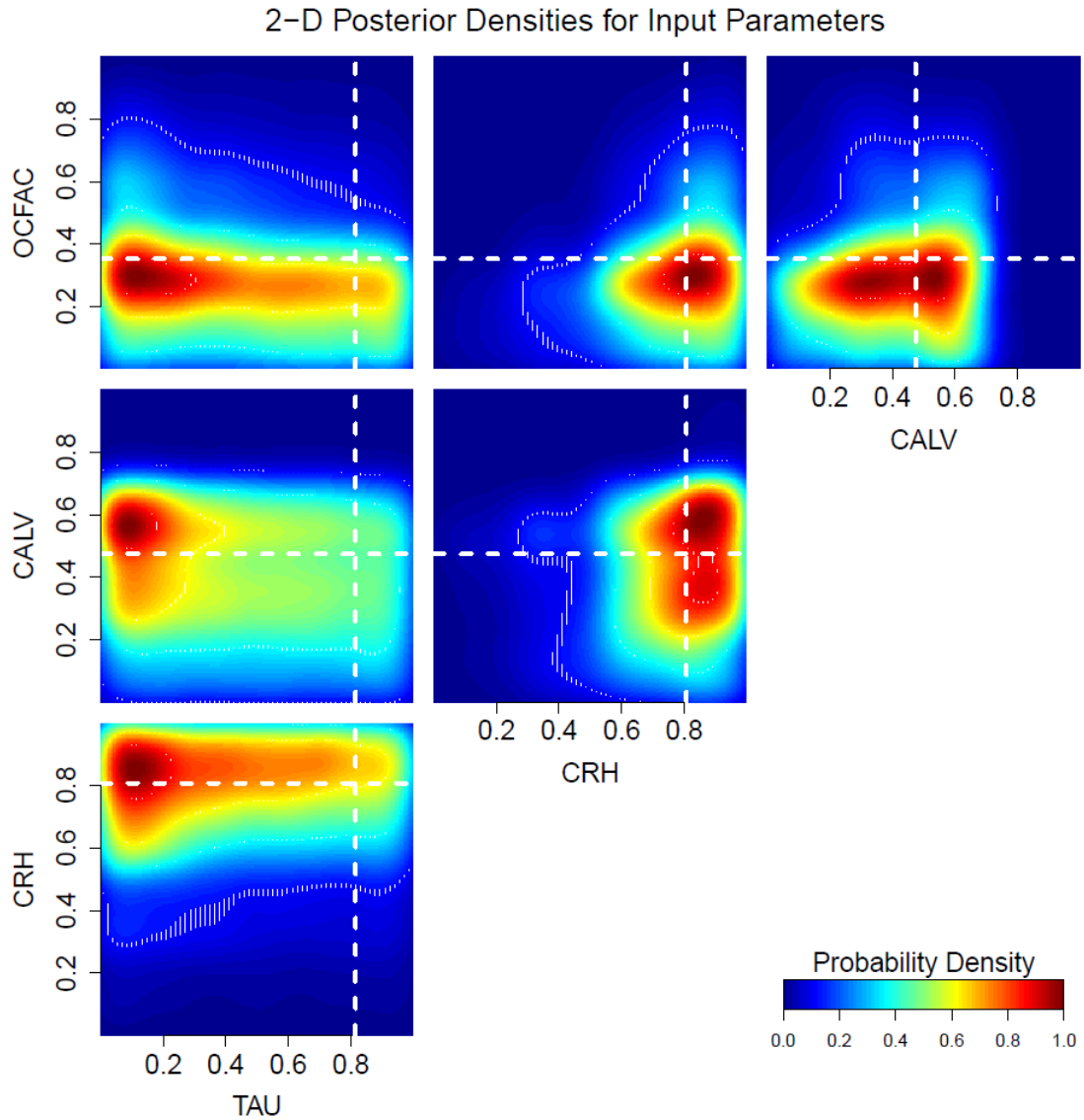
Figure 3: The pairwise joint posterior densities for the input parameters from the calibration results for the simulated example in Section 5.1. We plot only the following four parameters that we are most interested in: ocean sub-ice-shelf melt factor (OCFAC), calving factor (CALV), basal sliding coefficient (CRH), and asthenospheric relaxation e-folding time (TAU) (see Section 5.2 for parameter descriptions). The white dashed lines show the input parameter settings for the synthetic truth. The marginal densities peak around the assumed true values for the parameters. The lone exception is TAU, indicating that the modern ice coverage pattern is not informative about this parameter.
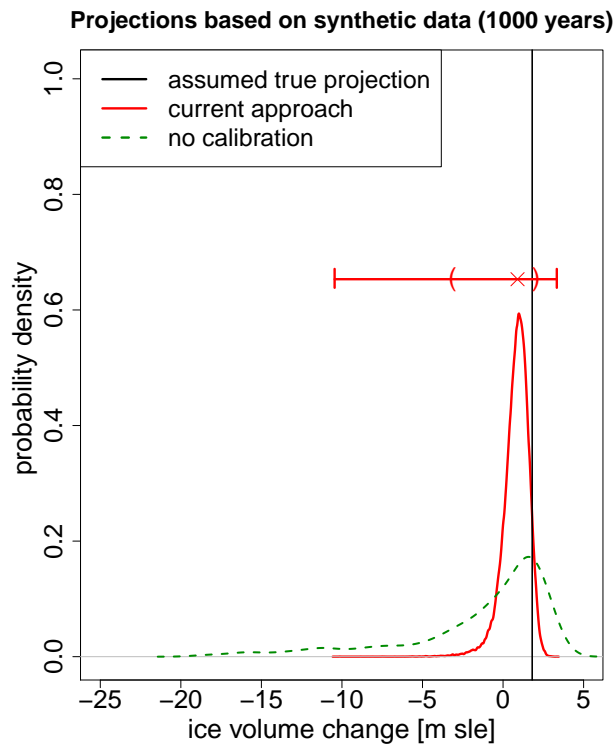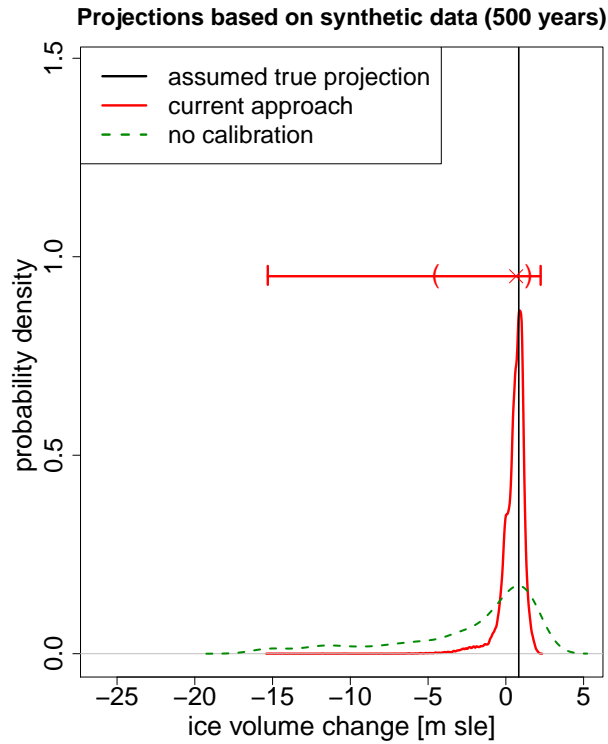
Figure 4: The ice volume change projections for 500 years (left panel) and 1000 years (right panel) from the simulated example described in Section 5.1 based on the calibration results (solid red lines) in Figure 3 and no calibration (dashed green lines). The vertical black line shows the true projection value generated by the synthetic truth. The parentheses on the horizontal bars represent 95% prediction intervals and the vertical bars the ranges. The slight bias in the mode of the predictive distribution for the volume changes for 1000 years is likely due to the bias for the posterior mode of TAU (see Figure 3).
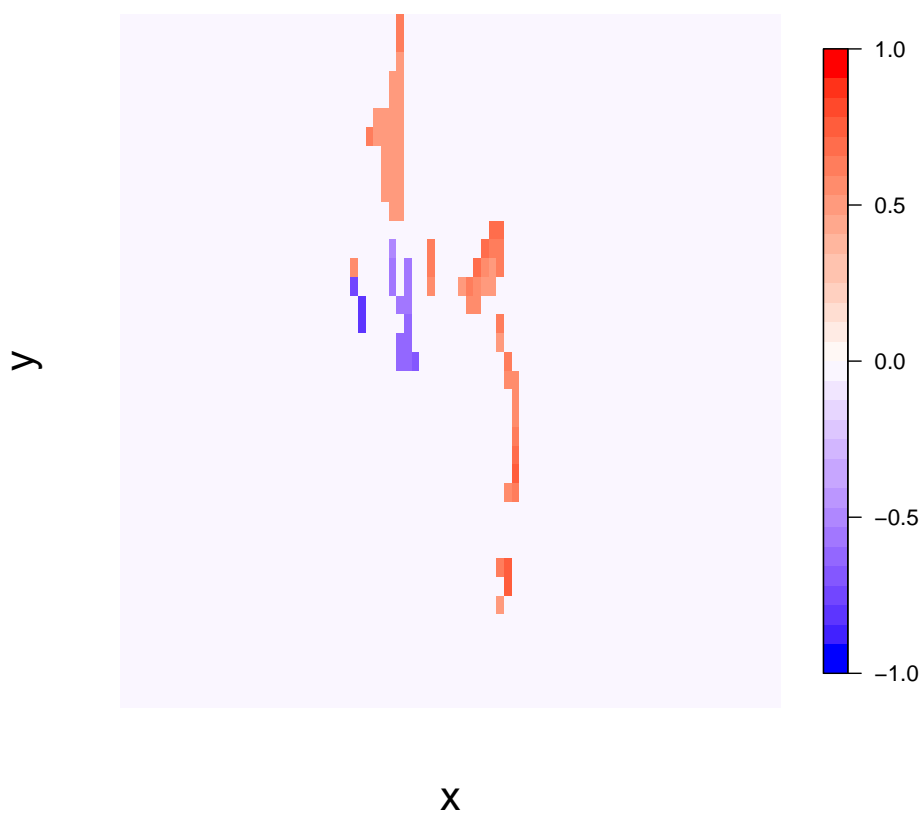
Figure 5: Estimated discrepancy between PSU3D-ICE model and the Bedmap2 observational dataset (Fretwell et al., 2013) by the procedure described in Section 4.3.
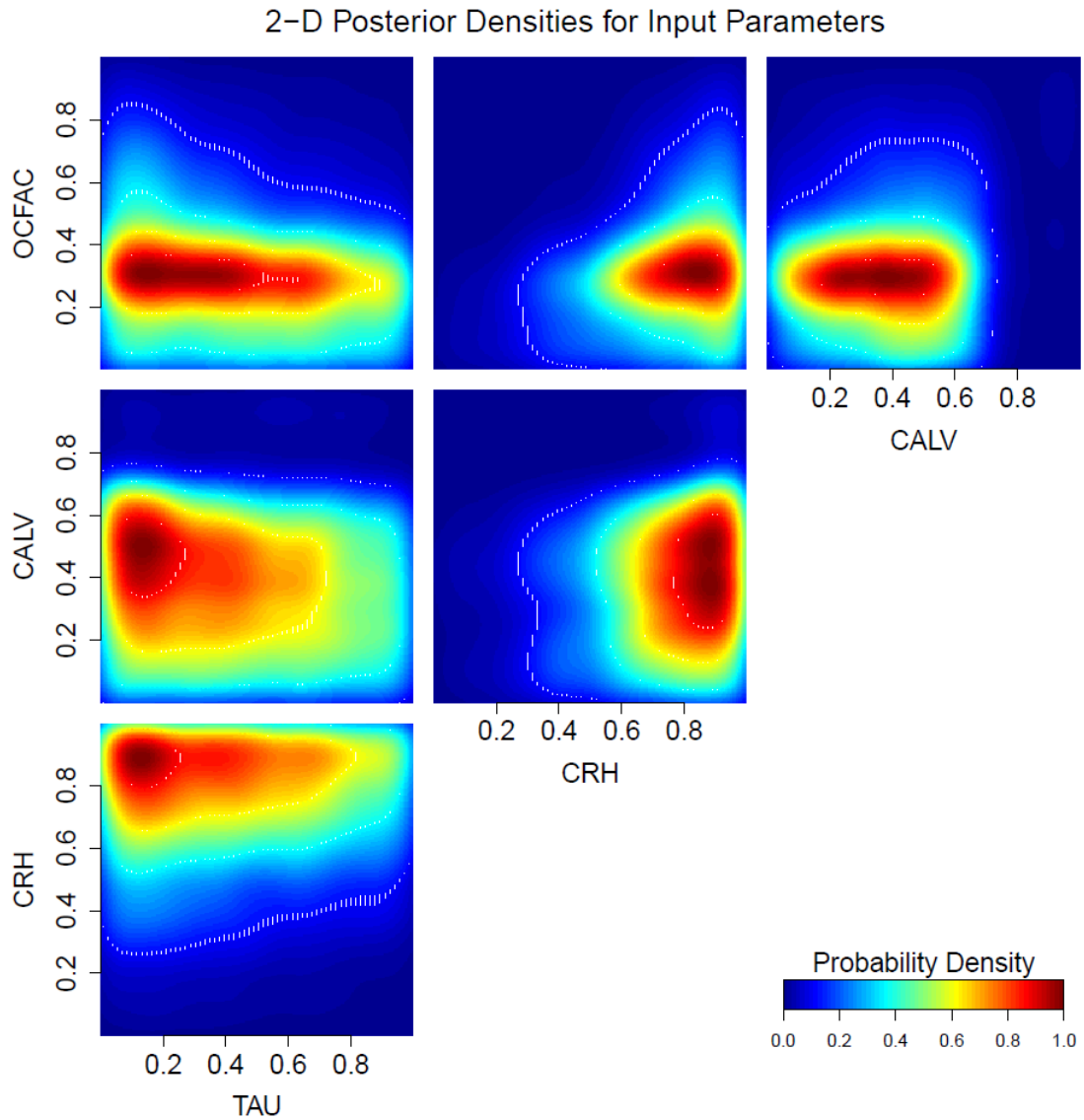
Figure 6: The pairwise joint posterior densities for the input parameters from the calibration results based on the real observational data described in Section 2. Again we plot only the following four important parameters: ocean sub-ice-shelf melt factor (OCFAC), calving factor (CALV), basal sliding coefficient (CRH), and asthenospheric relaxation e-folding time (TAU) (see Section 5.2 for parameter descriptions). Similar to the results in Figure 3, the posterior densities have tightly constrained high density regions except for TAU.

Projections based on observations (500 years)
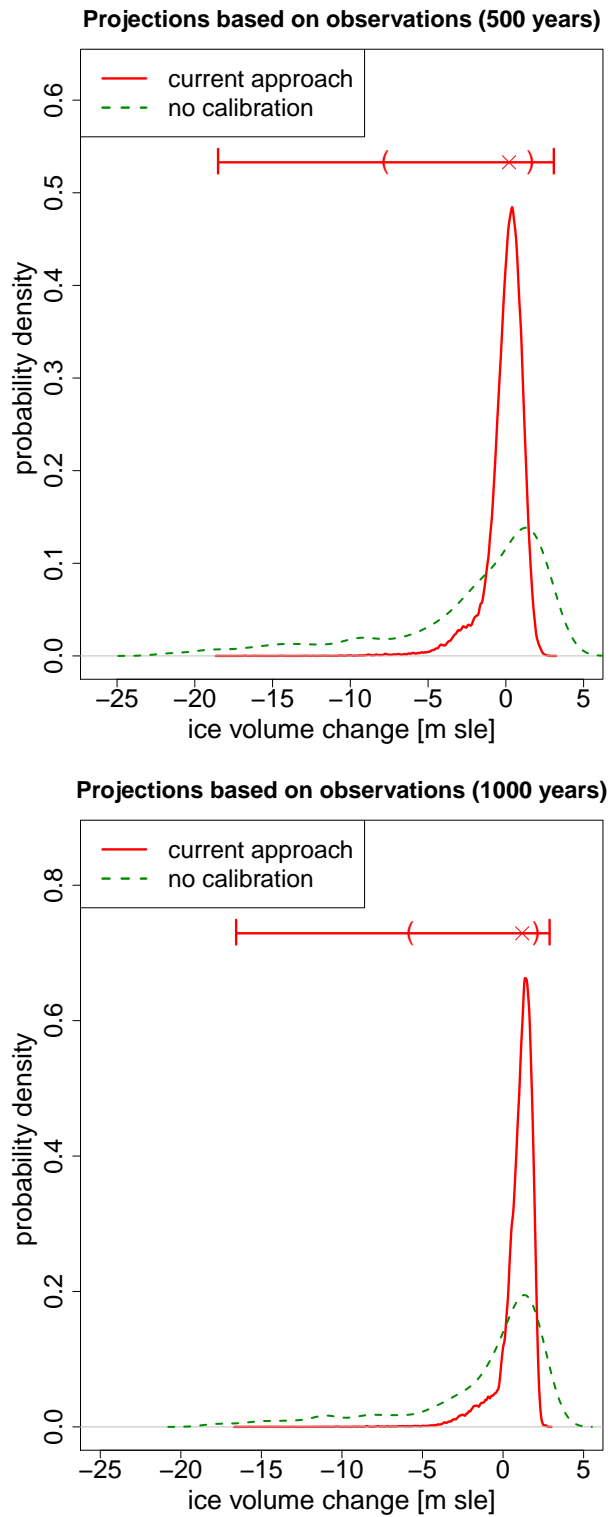
Projections based on observations (1000 years)

Figure 7: The ice volume change projections for 500 years (left panel) and 1000 years (right panel) based on the calibration results (solid red lines) using the real observational data shown in Figure 6 and no calibration (dashed green lines). The parentheses on the horizontal bars represent 95% prediction intervals and the vertical bars represent the ranges.